Chapter 6

Synthesis, Crystal Structure, and Physical Properties of the Perovskite Iridates

Yunqi Cai, Yan Li and Jinguang Cheng

Additional information is available at the end of the chapter

http://dx.doi.org/10.5772/61281

Abstract

Perovskite iridates have emerged as a new paradigm for studying the strongly correlated electron physics with strong spin-orbit coupling. The "113" alkaline-earth iridates $AIrO_3$ (A = Ca, Sr, Ba) display a rich variety of crystallographic and electronic states and are now attracting growing research interest. This chapter aims to provide an overview for these "113" iridates, including the materials' synthesis, crystal structure, major physical properties, and other interesting results such as the effects of pressure and chemical substitutions, as well as theoretical perspectives.

Keywords: Perovskite iridates, Spin-orbit coupling, Post-perovskite, Polytype, Semimetal

1. Introduction

The discoveries of high-transition-temperature superconductivity in cuprates and the colossal magnetoresistance in manganites made the first-row (3d) transition-metal oxides (TMOs) with perovskite-related structures the central topics of condensed matter physics over the past four decades. The strong electron–electron correlations intrinsic for these narrow-band 3d-electron systems are believed to be at the heart of rich physics. Following the general wisdom based on the 3d TMOs, the third-row (5d) counterparts having a spatially much extended 5d orbitals were expected to have much reduced electron–electron correlations, U, and broaden bandwidth, W, i.e. $U << W$, leading to a Pauli paramagnetic metallic ground state, Figure 1(a). Such an expectation, however, was recently found to be violated in many 5d-electron iridium oxides (iridates), such as Sr_2IrO_4 [1], in which an antiferromagnetic insulating ground state was instead observed. Recent studies have revealed that such discrepancy originates from the inherently strong spin-orbit coupling (SOC) for these heavy 5d elements, which have a typical

value of SOC, $\zeta_{SO} \approx 0.3–0.5$ eV, comparable with the magnitude of U and W, and thus cannot be treated as a negligible perturbation as in the 3d TMOs.

Since an unrealistically large U is required to open a Mott gap in Sr_2IrO_4, Figure 1(b), Kim et al. [2] proposed that the strong SOC splits the otherwise broad t_{2g} band of the octahedral-site, low-spin $Ir^{4+}(5d^5)$ array into a filled, low-energy $J_{eff} = 3/2$ quartet band and a half-filled, high-energy $J_{eff} = 1/2$ doublet band, Figure 1(c, e). A moderate Hubbard U can then open a Mott gap, leading to the SOC-driven $J_{eff} = 1/2$ Mott insulating state, Figure 1(d). Subsequent experimental [3] and theoretical [4] investigations have confirmed such a novel $J_{eff} = 1/2$ state in the strong SOC limit. Since then, the 5d TMOs have emerged as a new paradigm for studying the strongly correlated electron physics with strong SOC. In particular, the iridates have attracted special attention in that the combination of relativistic SOC and electron–electron correlations has been proposed to generate more exotic, unprecedented quantum states of matters, such as the strong topological insulators, Weyl semimetal, quantum spin liquids, and even unconventional superconductors [5].

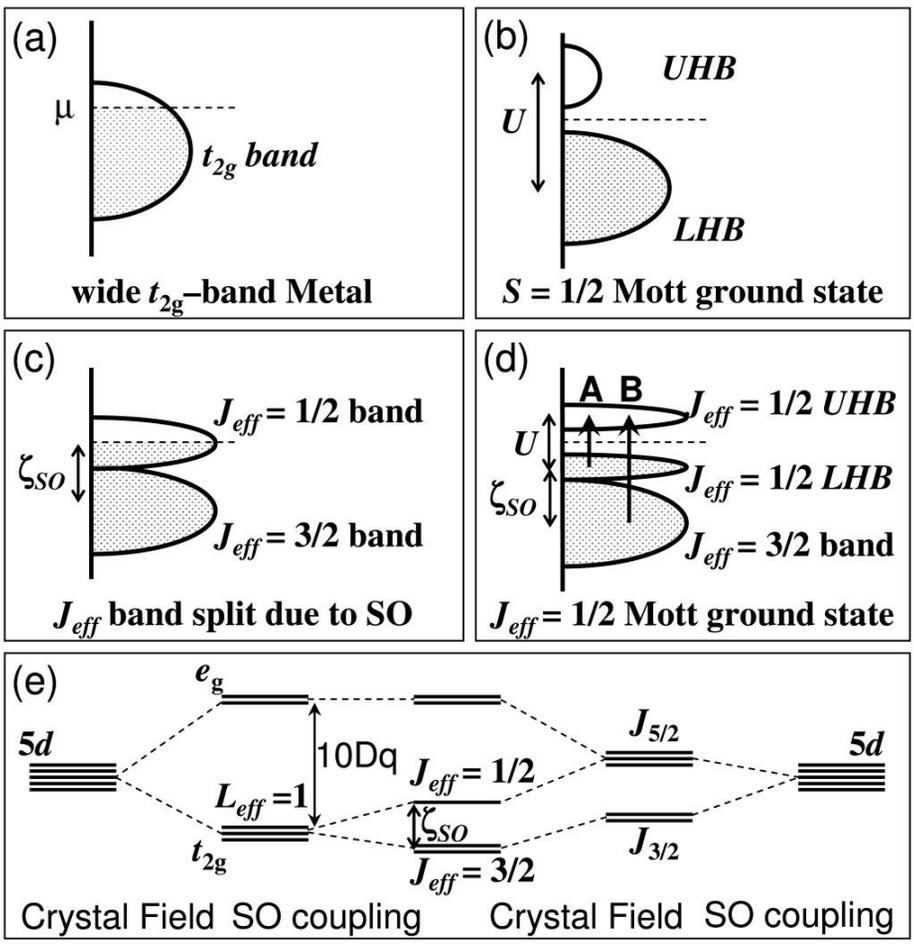

Figure 1. Schematic energy diagrams for the $5d^5$ (t_{2g}^5) configuration: (a) without SOC and U, (b) with an unrealistically large U but no SOC, (c) with SOC but no U, and (d) with SOC and U, (e) 5d level splitting by the crystal field and SOC. Adapted from Reference [2].

http://dx.doi.org/10.5772/61281

Since the importance of SOC was first recognized in Sr_2IrO_4, which is the $n = 1$ member of the Ruddlesden–Popper series $Sr_{n+1}Ir_nO_{3n+1}$ ($n = 1, 2, \infty$), these perovskite (Pv) iridates are currently archetypal systems for studying the interplay of SOC and electron–electron correlations. During the past few years, numerous studies have been performed on the single-layer Sr_2IrO_4 ($n = 1$) and bilayer $Sr_3Ir_2O_7$ ($n = 2$); for a review, see Reference [6]. With increasing the number of Pv layers n, the bandwidth of the $J_{eff} = 1/2$ band is expected to increase, and a dimensionality controlled insulator-to-metal transition is eventually realized in the orthorhombic Pv $SrIrO_3$ ($n = \infty$) [7]. Recent advances in this emergent field have turned much attention to the "113" alkaline-earth iridates $AIrO_3$ (A = Ca, Sr, Ba) with the Pv-related structures. However, in-depth investigations on these compounds are hindered to a great extent by the harsh synthesis conditions as well as their complex structural variations. For example, the above-mentioned orthorhombic Pv $SrIrO_3$ can only be stabilized in the bulk form under high-pressure and high-temperature (HPHT) conditions [8], or in the form of thin films by applying epitaxial strain [9]. Recent theoretical investigations proposed an intriguing topological semimetal state for the orthorhombic Pv phase [10]. When synthesized at ambient pressure, on the other hand, $SrIrO_3$ adopts a so-called six-layer (6H) polytype [8], which has been characterized as a non-Fermi-liquid metal approaching a ferromagnetic quantum critical point [11]. As the sister compounds of $SrIrO_3$, both $CaIrO_3$ and $BaIrO_3$ also display multiple structural polymorphs with interesting structural–property relationships. Depending on the synthesis conditions, $CaIrO_3$ can be stabilized in either the Pv or the post-perovskite (pPv) structure, which displays, respectively, a paramagnetic metal and an antiferromagnetic insulator ground states [12, 13]. Although the pPv $CaIrO_3$ was regarded as the $J_{eff} = 1/2$ Mott insulator [14], recent studies revealed a clear deviation from the ideal $J_{eff} = 1/2$ state due to the pronounced structural distortions [15]. In addition, in the field of geosciences, $CaIrO_3$ has been studied extensively as an analogy of $MgSiO_3$ to elucidate the mechanism of Pv to pPv transition at the boundary of Earth's lowermost mantle, or the D'' layer [16]. In the case of $BaIrO_3$, it also exhibits multiple structural polytypes with interesting structural–property relationship. At ambient pressure, $BaIrO_3$ adopts a nine-layer structure (9R). It is the first known ferromagnetic insulator among the 5d TMOs and exhibits intriguing charge-density-wave formation accompanying the ferromagnetic order [17, 18]. When treating the 9R phase under different pressures, three more polytypes, i.e. 5H, 6H, and 3C, have been identified [19]. Following the sequence of 9R → 5H → 6H → 3C, their ground states change progressively from a weak ferromagnetic insulator with $T_c = 180$ K for 9R, through a ferromagnetic metal with $T_c = 50$ K for 5H, and an exchange enhanced non-Fermi-liquid metal for 6H approaching a ferromagnetic quantum critical point, finally to a Pauli paramagnetic Fermi-liquid metal for 3C [20, 21]. These results demonstrate an intimate structure–property relationship that has been well documented in the 3d TMOs. A brief summary of the structural types and interesting physical properties for these "113" alkaline-earth iridates $AIrO_3$ (A = Ca, Sr, Ba) is given in Table 1.

Although there are many publications dealing with an individual compound, a monograph that provides a comprehensive overview for these "113" alkaline-earth iridates is still lacking to our knowledge. Taking into account the growing research interests on these iridates, it is imminent to summarize the currently available knowledge in a single chapter. Thus, this chapter aims to bring together the available information in literature for these "113" iridates.

In the following, we will give a comprehensive literature survey for each $AIrO_3$, covering the materials' synthesis, crystal structure, and major physical properties, as well as other interesting results such as the effects of chemical substitutions and theoretical investigations. Finally, we will give a brief concluding remark on the current research status and provide an outlook on the future research directions on these iridates.

Compound	Structure type	Interesting physical properties
$CaIrO_3$	pPv	AF insulator with T_N = 110 K, stripe-type AF order with spin canting;
	Pv	PM semimetal with possible Dirac node protected by reflection symmetry
$SrIrO_3$	6H	Exchange enhanced PM metal with nFL behaviors due to proximity to a FM QCP
	Pv	PM semimetal with possible Dirac node protected by reflection symmetry
$BaIrO_3$	9R	Weak FM insulator with a simultaneous CDW formation below $T_c \approx 180$ K
	5H	Weak FM metal with $T_c \approx 50$ K
	6H	Exchange enhanced PM metal with nFL behaviors due to proximity to a FM QCP
	3C	FL PM metal

AF: Antiferromagnetic; PM: Paramagnetic; FM: Ferromagnetic; FL: Fermi liquid;

nFL: non Fermi liquid; CDW: Charge density wave; QCP: Quantum critical point

Table 1. A summary of the "113" Alkaline-earth iridates $AIrO_3$ (A=Ca, Sr, Ba)

2. $CaIrO_3$

$CaIrO_3$ has two different orthorhombic polymorphs, i.e. the layered pPv structure with space group *Cmcm* and the $GdFeO_3$-type Pv structure with space group *Pbnm*. These two compounds have been known since 1960s [22, 23] and received significant attention from geologists since 2004 as an analogy of $MgSiO_3$, the main constituent mineral of the Earth's lower mantle [16, 24]. More recently, they have emerged as important correlated 5d-electron systems with strong SOC [14, 25]; the strong local distortion in pPv $CaIrO_3$ makes it a model system to investigate the interplay of non-cubic crystal field splitting and SOC [15], while the orthorhombic Pv $CaIrO_3$ might be considered as an intriguing semimetal with symmetry-protected Dirac points [26].

2.1. Synthesis

There are some discrepancies in literature regarding the synthesis of pPv $CaIrO_3$ at ambient pressure. In the earlier studies [12, 22], it was reported that single-phase pPv phase cannot be obtained at ambient pressure through a solid-state reaction from $CaCO_3$ and IrO_2 in air. Recently, Harai et al. [27] reported that pure pPv $CaIrO_3$ can be prepared by heating the stoichiometric mixture of CaO and IrO_2 powders sealed in an evacuated silica tube at 1000°C

http://dx.doi.org/10.5772/61281

over 20 h. On the other hand, since the pPv structure is a high-pressure phase, pPv $CaIrO_3$ can be readily obtained by utilizing HPHT synthesis. For example, Ohgushi et al. [25] reported the synthesis of single-phase pPv $CaIrO_3$ at 4 GPa and 1150°C.

Needle-shaped pPv $CaIrO_3$ single crystals have been reported to grow out of the $CaCl_2$ flux. By adopting a tenfold flux and a relatively low soaking temperature of 836 and 950°C, respectively, Sugahara et al. [28] and Hirai et al. [29] obtained tiny single crystals for the purpose of crystal-structure refinements. On the other hand, Ohgushi et al. [14] seems to grow sizable pPv $CaIrO_3$ single crystals for anisotropic magnetic property measurements by employing a higher flux molar ratio (16:1) and a higher soaking temperature of 1200°C. However, our attempts by using the latter approach ended up with Ca_2IrO_4 rather than the pPv $CaIrO_3$.

Because Pv $CaIrO_3$ is a metastable phase, it cannot be synthesized via a solid-state reaction route at ambient pressure. Alternatively, Sarkozy et al. [12] reported the preparation of pure Pv phase by thermal decomposition at 650–700°C in air of the hydroxide intermediate $CaIr(OH)_6$, which can be obtained according to the following wet-chemical reaction scheme:

$$K_2IrCl_6 \xrightarrow{H_2O} IrCl_6^{2-} \xrightarrow{KOH,\,pH\,10-12} Ir(OH)_6^{2-} \xrightarrow{Ca^{2+}} CaIr(OH)_6 \downarrow .$$

By following this approach, we obtained nearly single-phase Pv $CaIrO_3$ with a trace amount of IrO_2 (0.2 wt.%) and Ca_2IrO_4 (1.3 wt.%) [30]. Recently, Kojitani et al. [31] determined a large positive Clapeyron slope for the pPv/Pv transition of $CaIrO_3$, i.e. Pv structure is the high-temperature phase of pPv. Thus, Pv $CaIrO_3$ can be obtained by transforming pPv phase at higher temperature under given pressures. For example, Ohgushi et al. [13] have reported the synthesis of single-phase Pv $CaIrO_3$ at 1 GPa and 1450°C. In addition, thin films of Pv $CaIrO_3$ have recently been epitaxially stabilized on various substrates [26, 32].

2.2. Crystal structure

pPv $CaIrO_3$ As shown in Fig. 2(a), the crystal structure of pPv $CaIrO_3$ can be described as a pseudo-2D layered structure having IrO_6 octahedral sheets stacked alternatively with the Ca^{2+} ions along the crystallographic *b* axis. Within the octahedral sheets, IrO_6 octahedra share edges along the *a* axis to form rutile-type chains; these chains are then interconnected with each other via apical oxygen atoms along the *c* axis. Because of the significant interest in geosciences, the crystal structure of pPv $CaIrO_3$ have been thoroughly studied by several groups [28, 29]. To illustrate the peculiar features of pPv $CaIrO_3$, here we adopted the results given by Sugahara *et al.* [28] who refined the crystal structure based on the single-crystal X-ray diffraction (XRD) technique. The crystal structure was refined in an orthorhombic space group *Cmcm* (No. 63) with Ca at *4c* (0, y, 1/4), Ir at *4a* (0, 0, 0), O1 at *4c* (0, y, 1/4), and O2 at *8f* (0, y, z) sites, respectively. The obtained unit cell parameters are a = 3.147 Å, b = 9.866 Å, c = 7.302 Å, and V = 226.7 Å^3 at room temperature. The refined positional parameters and selected bond lengths and bond angles after Reference [28] are listed in Table 2. Within the buckled octahedral layer, the IrO_6 octahedral chains display an alternative rotation about the *a* axis,

resulting in Ir-O1-Ir bond angles of 134.3°. As a result, for a given octahedron the local *z* axis that is along the Ir-O1 bond deviates from the crystallographic *c* axis by about 23°. In addition, IrO_6 octahedra show a significant tetragonal compression, with two short Ir-O1 (1.978 Å) and four long Ir-O2 (2.066 Å) bonds. Octahedral-site distortions can be generally described by the orthorhombic vibrational modes $Q_2 = l_x - l_y$ and $Q_3 = (2l_z - l_x - l_y)/\sqrt{3}$, where l_x, l_y, l_z are the bond lengths for bonding along local *x*, *y*, *z* directions. In pPv $CaIrO_3$, the octahedral-site distortion corresponds to a negative mode of $Q_3 = -0.102$. For comparison, the PtO_6 octahedra in the pPv $CaPtO_3$ with a filled t_{2g}^6 manifold show a negligible $Q_3 = -0.001$. Such a comparison highlights a strong orbital-lattice coupling in pPv $CaIrO_3$ with low-spin t_{2g}^5 configuration for Ir^{4+} ions, for which the single hole would be expected to have a dominant $yz \pm izx$ orbital character [30], which has been confirmed recently by the resonant inelastic X-ray spectroscopy [15].

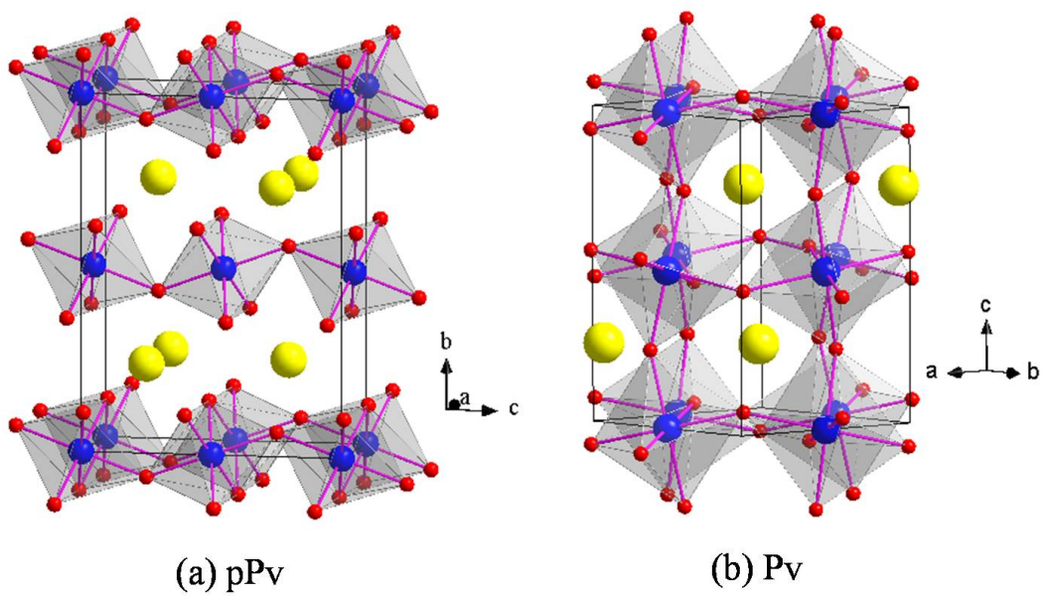

Figure 2. Crystal structure of $CaIrO_3$ polymorphs: (a) pPv and (b) Pv.

Pv $CaIrO_3$ As shown in Fig. 2(b), the crystal structure of Pv $CaIrO_3$ is built up from corner-shared IrO_6 octahedra in three dimensions with Ca cations in the interstitial positions. It has been known over 40 years that Pv $CaIrO_3$ adopts the $GdFeO_3$-type structure; however, structural refinements have not been performed until recently. We present here our Rietveld refinement results [30] based on the high-resolution synchrotron XRD on polycrystalline Pv $CaIrO_3$ prepared with the wet-chemical method mentioned above. The crystal structure was refined in space group *Pbnm* (No. 62) with Ca at *4c* (*x*, *y*, 1/4), Ir at *4b* (0.5, 0, 0), O1 at *4c* (*x*, *y*, 1/4) and O2 at *8d* (*x*, *y*, *z*) sites, respectively. The lattice parameters at room temperature are determined as a = 5.35046 Å, b = 5.59291 Å, c = 7.67694 Å, and V = 229.73 $Å^3$. The obtained positional parameters and selected bond lengths and bond angles after Reference [30] are listed in Table 3. In comparison with the pPv phase, the IrO_6 octahedra are less distorted with three sets of Ir-O distances of 2.006 Å, 2.020 Å, and 2.038 Å; the average Ir-O distance of 2.021 Å is

http://dx.doi.org/10.5772/61281

consistent with the ionic radii sum for Ir^{4+} (0.625 Å) and O^{2-} (1.40 Å). The averaged Ir-O-Ir bond angle is about 145.5° in the Pv phase.

Atom	Site	*x*	*y*	*z*	B_{iso} (Å²)
Ca	4c	0	0.7492	1/4	0.40
Ir	4a	0	0	0	0.32
O1	4c	0	0.0779	1/4	0.70
O2	8f	0	0.3658	0.4452	0.79
Ir-O1 (×2)	1.978		Ir-O1-Ir	134.3	
Ir-O2 (×4)	2.066		O1-Ir-O2	86.3	
<Ir-O>	2.037		O1-Ir-O2	93.7	
Ir-Ir (×2)	3.1472				
Ir-Ir (×2)	3.651				

Table 2. Refined positional parameters and selected bond lengths (Å) and bond angles (°) for pPv $CaIrO_3$ from single-crystal XRD [28]: space group *Cmcm* (No. 63), *a* = 3.1472 Å, *b* = 9.8655 Å, *c* = 7.3018 Å, *V* = 226.71 Å³, Z = 4.

Atom	Site	*x*	*y*	*z*	B_{iso} (Å²)
Ca	4c	-0.01403	0.05962	1/4	0.71
Ir	4b	0.5	0	0	0.27
O1	4c	0.10487	0.47110	1/4	0.92
O2	8d	0.69257	0.30488	0.05602	1.07
Ir-O1 (×2)	2.006		Ir-O1-Ir	146.15	
Ir-O2 (×2)	2.020		Ir-O2-Ir	144.95	
Ir-O2 (×2)	2.038				
<Ir-O>	2.021				

Table 3. Refined positional parameters and selected bond lengths (Å) and bond angles (°) for Pv $CaIrO_3$ from powder XRD[30]: space group *Pbnm* (No. 62), *a* = 5.35046 Å, *b* = 5.59291 Å, *c* = 7.67694 Å, *V* = 229.73 Å³, Z = 4.

2.3. Physical properties

pPv $CaIrO_3$ It is an antiferromagnetic insulator with $T_N \approx 110$ K. Due to the difficulty in obtaining single-phase samples, the physical properties of pPv $CaIrO_3$ were not characterized until 2006 by Ohgushi et al. [25], who first reported its electrical transport and magnetic properties on polycrystalline samples synthesized under HPHT conditions. As shown in Figure 3, its resistivity ϱ(T) increases quickly upon cooling, following the Arrhenius-type behaviour, i.e. $\varrho(T) = \varrho_0 \exp(\Delta/T)$, with the activation energy $\Delta = 0.17$ eV; magnetic susceptibility $\chi = M/H$ exhibits a sharp transition at $T_N = 115$ K, below which a weak ferromagnetic moment of ~ 0.04 μ_B/Ir was observed from the isothermal magnetization curve. In addition, a huge coercive field

$H_c \approx 4$ T was evidenced at low temperatures. Density functional calculations by Subedi [33] demonstrated that the inclusion of SOC can split the t_{2g} bands into fully filled $J_{eff} = 3/2$ bands and half-filled $J_{eff} = 1/2$ bands, as shown schematic in Figure 1(c), and that both SOC and moderate U are required to reconcile the experimentally observed Mott insulating behaviour. By performing the resonant X-ray diffraction at the L absorption edges of pPv $CaIrO_3$ single crystals, Ohgushi et al. [14] determined its magnetic structure as a stripe-type antiferromagnetic order, i.e. the Ir moments are aligned parallel along the *a* axis and antiparallel along the *c* axis with a canted ferromagnetic component along the *b* axis. Bogdanov et al. [34] carried out *ab initio* quantum chemical calculations and reproduced such a striped antiferromagnetic structure. Moreover, their calculations predicted a strong antiferromagnetic exchange interaction of $J_c = 121$ meV through the corner-shared path along the *c* axis, and a weak nearest-neighbour ferromagnetic coupling of $J_a \approx -7.3$ meV within the edge-shared chains along the *a* axis. In this regard, pPv $CaIrO_3$ can be regarded as a $J_{eff} = 1/2$ quasi-1D antiferromagnet. Although the above results suggested that a $J_{eff} = 1/2$ ground state is realized in pPv $CaIrO_3$, first-principles calculations [33, 34] evidenced significant deviations from the ideal $J_{eff} = 1/2$ state with highly uneven admixture of the t_{2g} components due to the pronounced tetragonal distortion. In agreement with these calculations, a very recent resonant inelastic X-ray scattering (RIXS) study by Sala et al. [15] confirmed the departure from the $J_{eff} = 1/2$ state. By analyzing the RIXS spectrum, they estimated the effective tetragonal crystal field splitting $\Delta = -0.71$ eV and the SOC $\zeta_{SO} = 0.52$ eV, from which a ground state wave function $|\mathbf{0}, \pm\rangle = \mp \mathbf{0.32}|\boldsymbol{xy}, \mp\rangle + \mathbf{0.67}(|\boldsymbol{yz}, \pm\rangle \mp \boldsymbol{i}|\boldsymbol{zx}, \pm\rangle)$ with a dominant yz±izx orbital character was derived.

The Mott insulating nature of quasi-2D pPv $CaIrO_3$ have motivated Ohgushi et al. [25] to metallize it via the carrier doping. They successfully prepared a series of hole-doped $Ca_{1-x}Na_xIrO_3$ ($0 \le x \le 0.37$) with pPv structure under HPHT conditions and realized a filling-control antiferromagnetic insulator to paramagnetic metal transition around $x = 0.3$, near which, however, no superconductivity was observed. Nevertheless, anomalous properties such as the non-Fermi-liquid behaviour and positive magnetoresistance violating Kohler's rule were observed for the metallic samples. In the same report, attempt of electron doping via Y^{3+} substitutions for Ca^{2+} was unsuccessful due to the formation of pyrochlore phase. In a recent work by Gunasekera et al. [35], however, Y-substituted $Ca_{1-x}Y_xIrO_3$ ($0 \le x \le 0.5$) samples with pPv structure were successfully fabricated via a conventional solid-state reaction route at ambient pressure. Similar with the Na^+-doped case, about 30%-Y^{3+} doping can also drive an insulator-to-metal transition; superconductivity was not observed either in this case. In striking contrast with the gradual suppression of T_N by Na doping, surprisingly, T_N remains unchanged upon Y substitutions up to 50%, except that the magnitude of ac susceptibility peak decreases about one order. Further experiments are needed to exclude the possibility that the magnetic order arises from the minor $CaIrO_3$ phase. Anyhow, metallization of the quasi-2D pPv $CaIrO_3$ represents an interesting direction to pursue exotic electronic state in the vicinity of metal–insulator transition.

Pv $CaIrO_3$ In sharp contrast with the antiferromagnetic insulating ground state of pPv $CaIrO_3$, the Pv phase has been reported as a Pauli paramagnetic metal by Sarkozy et al. [12] in 1974.

http://dx.doi.org/10.5772/61281

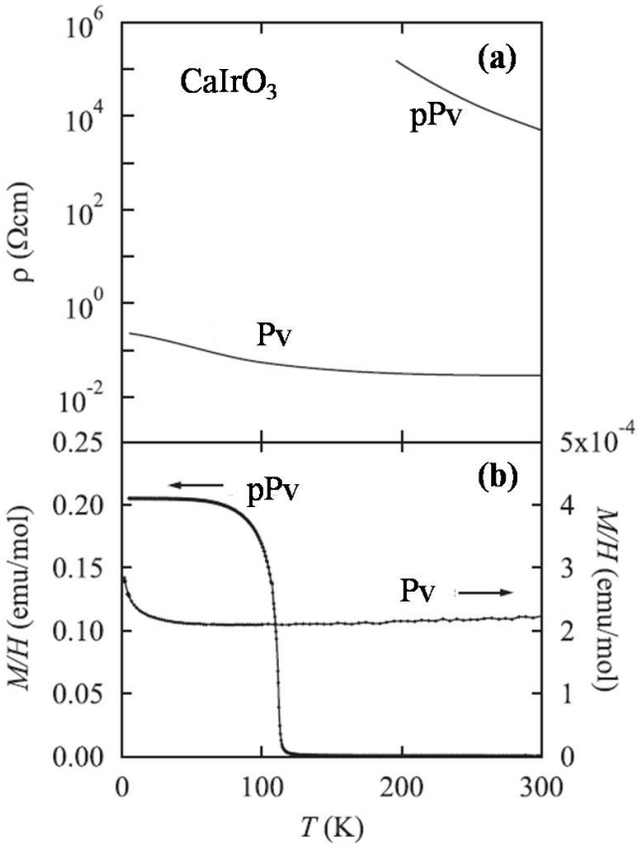

Figure 3. Temperature dependence of (a) resistivity ϱ(T) and (b) magnetic susceptibility M/H for the two polymorphs of $CaIrO_3$, pPv for post-perovskite and Pv for perovskite. Adapted from Reference [13].

Recent characterizations by Ohgushi et al. [13] on the dense pellets obtained via HPHT synthesis confirmed the paramagnetic nature, but the temperature dependence of resistivity shows bad metal behaviour with a non-diverge upturn at low temperatures, Figure 3. Such a bad metallic behaviour was reproduced on the epitaxially stabilized thin films grown on various substrates [26, 32], and has been ascribed to a semimetallic ground state with the conduction and valence band touching at Fermi level. The observations of a sign change and a nonlinear magnetic-field dependence of the Hall resistance are consistent with the coexistence of electron and hole charge carriers [26]. As discussed below for Pv $SrIrO_3$, the semimetallic state might originate from the symmetry-protected Dirac nodes around the Fermi level due to a combined effect of SOC and reflection symmetry of the *Pbnm* orthorhombic lattice. In light of the recent theoretical proposals for the orthorhombic Pv iridates discussed below, further experimental studies on the semimetallic Pv $CaIrO_3$ are highly desirable.

pPv versus Pv $CaMO_3$ (M = Ir, Rh, Ru) The distinct ground states of pPv and Pv $CaIrO_3$ reflect the intimate structural–property relationships. In addition to $CaIrO_3$, both $CaRuO_3$ [36] and $CaRhO_3$ [37] have also been reported to possess quenchable Pv and pPv polymorphs. Besides the importance in geosciences as analogy materials of $MgSiO_3$, these compounds with partially filled d-electron shells are important correlated electron systems with intriguing physical properties [37, 38]. In a similar manner as $CaIrO_3$, their ground states differ sharply as the

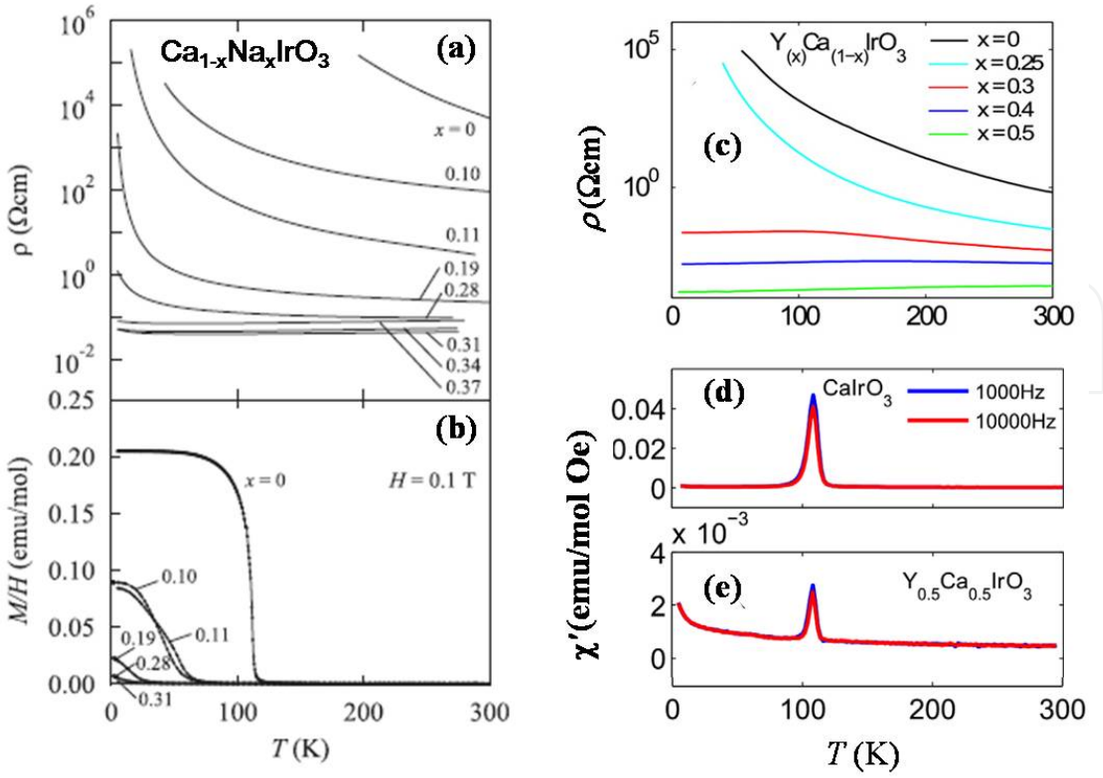

Figure 4. Insulator–metal transition in pPv $CaIrO_3$ induced by hole (Na^+) and electron (Y^{3+}) doping. (a, b) shows the temperature dependence of resistivity and magnetic susceptibility of $Ca_{1-x}Na_xIrO_3$. Adapted from Reference [25]; (c, d, e) show the temperature dependence of resistivity and ac magnetic susceptibility of $Ca_{1-x}Y_xIrO_3$. Adapted from Reference [35].

structure changes: Pv $CaRuO_3$ is a well-known exchanged-enhanced paramagnetic metal on the verge of a ferromagnetic instability, whereas the pPv phase is an antiferromagnetic insulator with $T_N = 270$ K [38]; Pv $CaRhO_3$ is a Pauli paramagnetic metal while the pPv phase is insulating and undergoes a canted antiferromagnetic transition below $T_N = 90$ K [37]. Current first-principles calculations for the pPv compounds failed to capture the correct ground state; it seems that in addition to electron–electron correlations, SOC also plays an essential role in producing the insulating ground state for these 4d and 5d-electron systems [39].

In addition to the interest in fundamental physics, the $CaIrO_3$ ceramics have also been investigated by Keawprak et al. [40] for the potential thermoelectric applications. They prepared both phases of $CaIrO_3$ with spark plasma sintering technique and evaluated their thermoelectric properties from room temperature up to 1023 K. The highest dimensionless figure of merit (ZT) reaches 0.02 and 0.003 for Pv and pPv phase, respectively.

3. $SrIrO_3$

Depending on the synthesis conditions, $SrIrO_3$ can form in two different structures, i.e. the monoclinically distorted 6H polytype and the orthorhombic $GdFeO_3$-type Pv structure [8]. The

http://dx.doi.org/10.5772/61281

former is a rare stoichiometric oxide exhibiting non-Fermi-liquid behaviours near a ferromagnetic quantum critical point [11]. The latter was recently found to be an exotic narrow-band semimetal that may harvest many topological and magnetic insulating phases [10, 41, 42].

3.1. Synthesis

The 6H phase can be readily prepared in the polycrystalline form at ambient pressure by sintering the stoichiometric mixture of $SrCO_3$ and IrO_2 (or Ir) at 900–1,100°C in air [8]. Single crystals of 6H phase with dimensions ~0.4 × 0.4 × 0.6 mm^3 have been grown in Pt crucibles with the $SrCl_2$ self-flux techniques [11]. The Pv phase is a HP form of $SrIrO_3$. Longo et al. [8] performed the first HPHT syntheses and established the temperature–pressure phase diagram for the 6H-Pv transformation of $SrIrO_3$. It was found that the 6H phase transforms to the Pv structure above 1,650°C at 2 GPa and above 700°C at 5 GPa. Recent HPHT syntheses of Pv $SrIrO_3$ were usually performed at 1,000–1,100°C and 5–6 GPa [43, 44]. For these samples, Rietveld refinements on the powder XRD patterns evidenced the presence of ~3–4 wt.% IrO_2 impurity. Since the Pv phase is metastable, it remains a challenge to obtain sizable bulk single crystals under HP conditions. However, Pv $SrIrO_3$ films and superlattices have been stabilized at ambient pressure via applying the epitaxial strain with various techniques, including the metalorganic chemical vapour deposition [9], pulsed laser deposition [45], and reactive oxide molecular-beam expitaxy [42]. As discussed below, given the tolerance factor $t < 1$, it is unusual for $SrIrO_3$ to adopt the 6H structure at ambient pressure. It was recently reported [46, 47] that the 6H structure of $SrIrO_3$ can be destabilized by partial substitution of M = Li, Fe, Co, Ni, Zn for Ir in $SrIr_{1-x}M_xO_3$ and converted to the Pv structure within a narrow composition range around $x = 0.2$. In these cases, it was suggested that the presence of e_g type orbitals on the M ions contributes to the breakdown of face-sharing octahedral dimmers in the 6H structure.

3.2. Crystal structure

6H $SrIrO_3$ The crystal structure of 6H $SrIrO_3$ was first determined by Longo et al. [8] as a monoclinic distortion of the hexagonal $BaTiO_3$ structure. The 6H hexagonal structure can be described as close-packed SrO_3 layers stacked perpendicular to the c axis in the sequence hcchcc, where h and c refer to hexagonal (ABAB...) and cubic (ABCABC...) close packing, respectively. The Ir atoms occupy the oxygen octahedra formed by the SrO_3 layers, and the IrO_6 octahedra share common faces across an h layer and common corners across a c layer. As a result, the above hcchcc stacking sequence results in two independent positions for the Ir atoms. As shown in Figure 5(a), two $Ir2O_6$ octahedra form pairs of face-shared octahedra that are joined by common corners to a plane of corner-sharing $Ir1O_6$ octahedra. Therefore, the 6H structure can be alternatively depicted as a stacking of layers of corner- (C) and face (F)-sharing IrO_6 octahedra in the sequence FCCFCC along the c axis.

In the original work by Longo et al., the oxygen positional parameters were not refined due to the low scattering of oxygen relative to Ir and Sr. Based on the neutron diffraction data, Qasim et al. [46] recently provided a full refinement on the crystal structure of 6H $SrIrO_3$ with $a = 5.6040$ Å, $b = 9.6256$ Å, $c = 14.1834$ Å, and $\beta = 93.202°$ in space group $C2/c$ (No. 15). The refined positional parameters and selected bond lengths and bond angles after Reference [46] are listed

in Table 4. In this structure, the $Ir1O_6$ octahedron has an average Ir-O distance of 2.006 Å typical of Ir^{4+} with the individual distances in a narrow range 1.987–2.038 Å. In contrast, the $Ir2O_6$ octahedra in the Ir_2O_9 dimers are not regular with a longer average Ir-O distance of 2.030 Å. The Ir2–Ir2 distance, 2.770 Å, is relatively short and close to the separation of 2.72 Å found in Ir metal, suggesting a strong Ir–Ir bonding across the common faces. Variable temperature XRD measurements on the 6H phase confirmed that the monoclinic structure is stable without any structural transition up to 1,000°C in air.

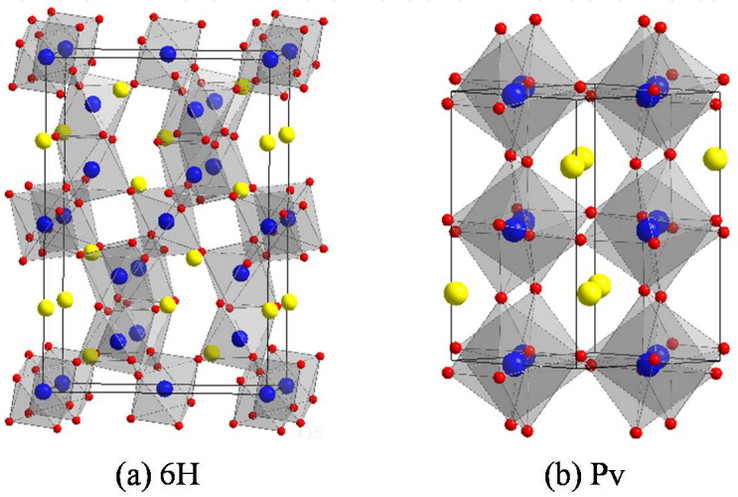

Figure 5. Crystal structure of $SrIrO_3$ polytypes: (a) 6H and (b) Pv.

Pv $SrIrO_3$ Similar as Pv $CaIrO_3$, it consists of a 3D network of corner-sharing IrO_6 octahedra that are cooperatively rotated and tilted about the pseudocubic [110] and [001] axes, Figure 5(b). Blanchard et al. [44] recently performed a thorough study on the crystal structure of Pv $SrIrO_3$ based on the synchrotron and neutron diffraction data. The crystal structure was refined in space group *Pbnm* (No. 62) with Sr at *4c* (*x*, *y*, 1/4), Ir at *4a* (0, 0, 0), O1 at *4c* (*x*, *y*, 1/4), and O2 at *8d* (*x*, *y*, *z*) sites, respectively. The lattice parameters at room temperature are determined as a = 5.60075 Å, b = 5.57115 Å, and c = 7.89601 Å. The obtained positional parameters and selected bond lengths and bond angles after Reference [44] are listed in Table 5. As can be seen, the individual IrO_6 octahedron is relatively rigid with three Ir–O distances being approximately equal. The average Ir–O distance at 300 K of 2.016 Å is consistent with the ionic radii sum for Ir^{4+} and O^{2-}. From the refined atomic coordinates, Blanchard et al. also estimated the two independent octahedral tilt angles, i.e. $\psi = 11.5°$ for out-of-phase tilt about the pseudocubic [110] axis, and $\varphi = 8.7°$ for in-phase tilt about the pseudocubic [001] axis, respectively. These tilting angles were found to be nearly temperature-independent below room temperature. The orthorhombic *Pbnm* structure was shown to persist over the temperature range 3–1,070 K.

6H-Pv transformation As pointed out by Longo et al. [8], $SrIrO_3$ and $SrMnO_3$ are the only $SrBO_3$ (B = Ti, Zr, Hf, Cr, Mo, Tc, Fe, Ru, Sn, Pb, Ce, Th) compounds that do not adopt the Pv structure at ambient pressure. Given the tolerance factor $t \leq 1$, the Pv structure would be stabilized for these compounds. However, $SrMnO_3$ has the 4H polytype structure with a

http://dx.doi.org/10.5772/61281

stacking sequence of hchc along the *c* axis, while $SrIrO_3$ crystallizes in the 6H polytype as mentioned above. It would appear that the hexagonal polytypes with their face-shared octahedra and trigonal crystal fields are stabilized by the outer electron configurations that allow for metal–metal bonding along the *c* axis. For example, in the case of low-spin Ir^{4+}, the trigonal crystal field of the hexagonal polytype should split the t_{2g}^5 orbitals to $e_{g\sigma}^0 e_{g\pi}^4 a_{1g}^1$, which allow for metal–metal bonding along the *c* axis via the half-filled a_{1g} orbitals. Thus, the 6H $SrIrO_3$ and 4H $SrMnO_3$ can be regarded as a compromise between the continuous face-shared chains of the 2H polytype and the geometrically favoured Pv structure. Since high pressure prefers the cubic close packing with a higher density than the hexagonal close packing, 6H $SrIrO_3$ transforms to the Pv structure under high-pressure conditions with a ~3% volume reduction.

Atom	Site	*x*	*y*	*z*	B_{iso} (Å^2)
Sr1	4e	0	0.0092	1/4	0.0285
Sr2	8f	0.0122	0.6667	0.0957	0.0482
Ir1	4a	0	0	0	0.0478
Ir2	8f	0.9820	0.6660	0.84698	0.0459
O1	4e	0	0.4981	1/4	0.0584
O2	8f	0.2411	0.2649	0.2603	0.0287
O3	8f	0.8112	0.4077	0.0474	0.0572
O4	8f	0.9407	0.1544	0.4087	0.0535
O5	8f	0.3238	0.4204	0.1058	0.0586
Ir1-O3 (×2)	2.038	Ir1-O3-Ir2	149.6		
Ir1-O4 (×2)	1.987	Ir1-O4-Ir2	158.8		
Ir1-O5 (×2)	1.994	Ir1-O5-Ir2	149.3		
<Ir1-O>	2.006				
Ir2-O1	2.100	Ir2-O1-Ir2	82.5		
Ir2-O2	2.055	Ir2-O1-Ir2	85.1		
Ir2-O2	2.040				
Ir2-O3	1.974				
Ir2-O4	1.957				
Ir2-O5	2.051				
<Ir2-O>	2.030				
Ir2-Ir2	2.770				

Table 4. Refined positional parameters and selected bond lengths (Å) and bond angles (°) for 6H $SrIrO_3$ from neutron diffraction [46]: space group *C*2/*c* (No. 15), a = 5.60401 Å, b = 9.6256 Å, c = 14.1834 Å, β = 93.202°, V = 763.89 Å^3, Z = 12.

Atom	Site	*x*	*y*	*z*	B_{iso} (Å^2)
Sr	4c	-0.0068	0.4687	1/4	0.019
Ir	4a	0	0	0	0.017
O1	4c	0.0718	0.0049	1/4	0.019
O2	8d	0.2126	0.2877	-0.0369	0.022
Ir-O1 (×2)	2.015	Ir-O1-Ir	156.92		
Ir-O2 (×2)	2.018	Ir-O2-Ir	156.22		
Ir-O2 (×2)	2.018				
<Ir-O>	2.017				

Table 5. Refined positional parameters and selected bond lengths (Å) and bond angles (°) for Pv $SrIrO_3$ from neutron diffraction [44]: space group *Pbnm* (No. 62), a = 5.60075 Å, b = 5.57115 Å, c = 7.89601 Å, V = 246.376 Å^3, Z = 4.

3.3. Physical properties

6H $SrIrO_3$ Although the 6H $SrIrO_3$ has been synthesized more than 50 years ago, its physical properties were not characterized in detail until 2007 by Cao et al. [11], who reported the magnetic, electrical transport, and calorimetric properties of 6H $SrIrO_3$ single crystals grown out of the $SrCl_2$ flux. The primary results are summarized in Figure 6. Magnetic susceptibility $\chi(T)$ measurements evidenced no long-range magnetic order down to 1.7 K, but exhibited at low temperatures strong enhancements that diverge as $\chi \propto T^{\gamma}$ with $1/2 < \gamma < 1$, suggesting the proximity to a ferromagnetic instability. The isothermal magnetization $M(H)$ at 1.7 K indeed displays a saturation behaviour at $H \sim 3$ T, yet the saturation moment is very small, being less than 0.03 μ_B/Ir. The low-temperature specific heat $C(T)$ exhibits a pronounced $-T\log T$ dependence, which is characteristic of non-Fermi-liquid systems. Such a $C/T \sim -\log T$ behaviour can be readily enhanced in low applied fields up to 1.1 T, vanishes for $H > 2$ T, and eventually changes to a $T^{3/2}$ power law expected for a ferromagnetically ordered state at $H = 8$ T. In accordance with the $C(T)$ results, both the c-axis resistivity, ϱ_c, and the ab-plane resistivity, $\varrho_{ab}(T)$, follow a non-Fermi-liquid $T^{3/2}$ dependence over a wide temperature range up to 120 K under zero field, while a Fermi-liquid T^2 behaviour is restored upon applying an external field $H \geq 5$ T. Taking into account all these observations, 6H $SrIrO_3$ can be regarded a rare example of stoichiometric oxide that exhibits non-Fermi-liquid behaviours near a ferromagnetic quantum critical point. As will be shown explicitly in $BaIrO_3$, such a quantum critical point can be realized via subtle structural variations.

Pv $SrIrO_3$ In the original work by Longo et al. [8], Pv $SrIrO_3$ has been described as a Pauli paramagnetic metal. In 2008, Zhao et al. [43] reinvestigated the physical properties of Pv $SrIrO_3$ bulk sample prepared under 5 GPa and 1,000°C. They observed two characteristic temperatures $T^* \approx 170$ K and $T_{MI} \approx 44$ K: at T^*, the paramagnetic susceptibility $\chi(T)$ starts to increase with temperature, and the resistivity $\varrho(T)$ exhibits a slope change, followed below T^* by the presence of unusual linear field dependence positive magnetoresistance (MR) that reaches about 12% at 5 K and 7 T; a broad metal–insulator transition was observed at T_{MI}. However, these observations are largely disapproved by the very recent work of Blanchard et

http://dx.doi.org/10.5772/61281

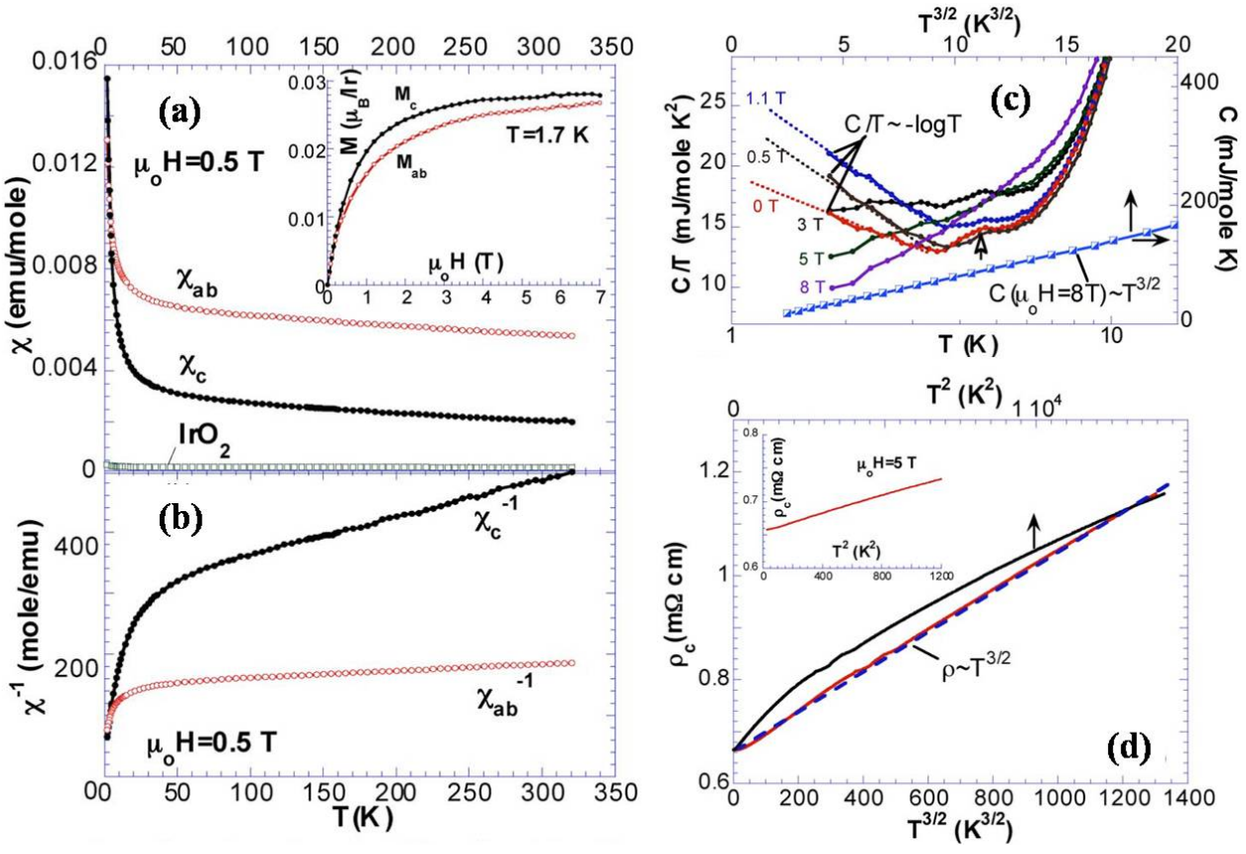

Figure 6. Physical properties of 6H $SrIrO_3$ single crystal. Adapted from Reference [11]. (a, b) show the temperature dependence of magnetic susceptibility measured along the *c* axis and *ab* plane, inset of (a) shows the magnetization curve at 1.7 K. (c) shows the specific heat C(T) data illustrating the $C/T \sim -\log T$ behaviour. (d) shows the resistivity following the $T^{3/2}$ behaviour.

al. [44], who studied the bulk samples prepared under 6 GPa and 1,100°C. As shown in Figure 7, it was found in the latter work that ϱ(*T*) exhibits metallic conductivity down to 2 K, following Fermi-liquid T^2 dependence between 2 and 30 K, without showing an upturn at low temperature. In addition, they observed a smaller positive MR up to 2% at 7 *T* and 2–50 K. These discrepancies might originate from the polycrystalline nature of the studied samples, in which the extrinsic effects such as the grain boundary and impurities can largely influence the transport properties. As mentioned above, Pv $SrIrO_3$ films of single-crystal quality can be stabilized via applying epitaxial strain. The resistivity upturn at low temperatures have been frequently observed in these thin films [9, 48], but the upturn temperature displays a broad distribution, in support of an extrinsic property due to weak Anderson localization. Nevertheless, such sensitivity to defects reflects the bad metal character of semimetallic Pv $SrIrO_3$ approaching the boundary of metal–insulator transition.

As the end member of the Ruddlesden–Popper series $Sr_{n+1}Ir_nO_{3n+1}$ (n = 1, 2, ∞), Pv $SrIrO_3$ has recently attracted much attention due to the presence of nontrivial features within the J_{eff} = 1/2 bands. Density-functional theory first-principles calculations by Carter et al. [10] found that in the strong SOC limit the bands near the Fermi energy are mostly composed of J_{eff} = 1/2 states. Interestingly, they found a node near the U point, Figure 8(a), thus revealing the semimetallic

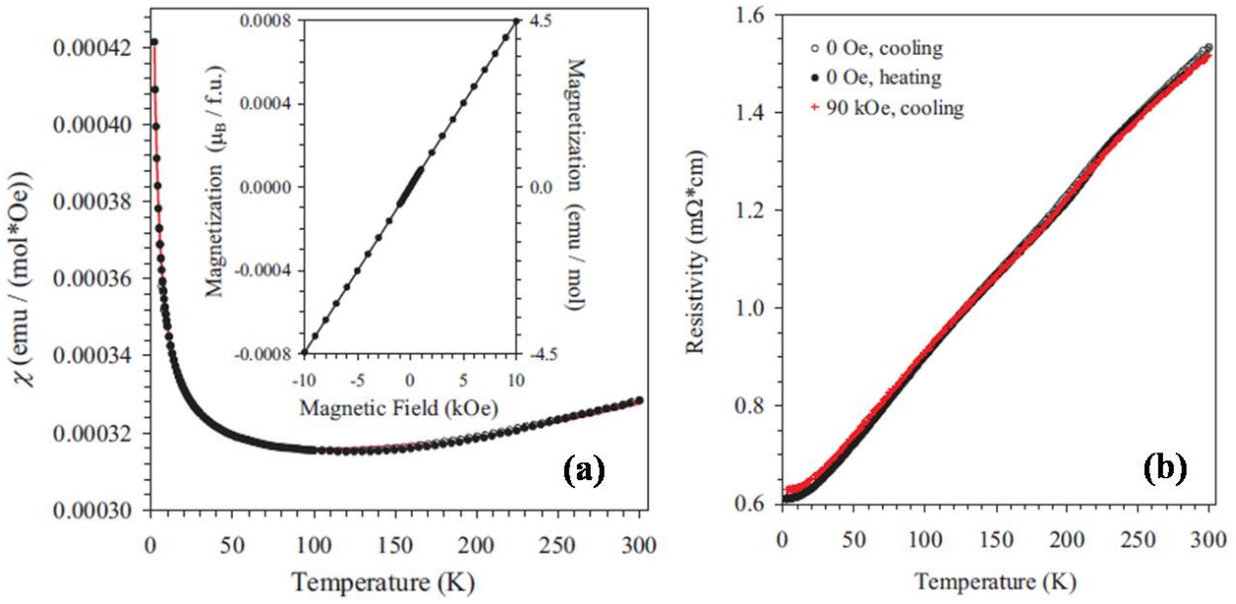

Figure 7. Temperature dependence of (a) magnetic susceptibility and (b) resistivity of Pv $SrIrO_3$. Adapted from Reference [44].

nature of Pv $SrIrO_3$. By constructing a tight-binding model, they confirmed the presence of a line node near the U point in the Brilloiun zone, and further shown that the line node originates from the reflection symmetry of the crystal structure at the z = 1/4 and 3/4 planes presented in the orthorhombic *Pbnm* space group. Since the line node is protected by the underlying lattice symmetry, it has been further proposed that perturbations breaking the sublayer reflection symmetry can lift the line node and convert the system into an insulating phase; the system may become a strong topological insulator at a certain point. In addition, as shown in Figure 8(b), magnetically ordered metallic and insulating phases have also been proposed to arise in the U versus SOC phase diagram of Pv $SrIrO_3$ [41]. Moreover, Chen et al. [49] further proposed that the presence of reflection symmetry in orthorhombic Pv iridates may realize a novel class of topological crystalline metals with zero-energy surface states at certain planes.

Recent angle-resolved photoemission spectroscopy on Pv $SrIrO_3$ films by Nie et al. [42] has uncovered such an exotic semimetallic state with very narrow bands near the Fermi surface consisting of heavy hole-like pockets around ($\pm\pi$, 0) and (0, 0) and light electron-like pockets at ($\pm\pi/2$, $\pm\pi/2$). Surprisingly, the bandwidth of Pv $SrIrO_3$ is found to be narrower than that of Sr_2IrO_4, in contrary to the general expectations of broaden bandwidth with increasing dimensionality [7]. Since the semimetallic ground state has been confirmed experimentally, it is of particular interest to achieve the proposed topological and/or magnetic states via tuning the SOC, U, and/or lattice symmetry. In this regard, Matsuno et al. [45] have made an important step towards these exotic phases; they tailored a spin-orbit magnetic insulator out of the semimetallic state via controlling the dimensionality of [$(SrIrO_3)_m$, $SrTiO_3$] superlattices. By utilizing HPHT synthesis, we prepared a series of Sn-doped $SrIr_{1-x}Sn_xO_3$ orthorhombic perovskites. We found that substitutions of isovalent, nonmagnetic Sn^{4+} for Ir^{4+} ions lead to a breakdown of the semimetallic state, and convert the paramagnetic, semimetallic ground state

http://dx.doi.org/10.5772/61281

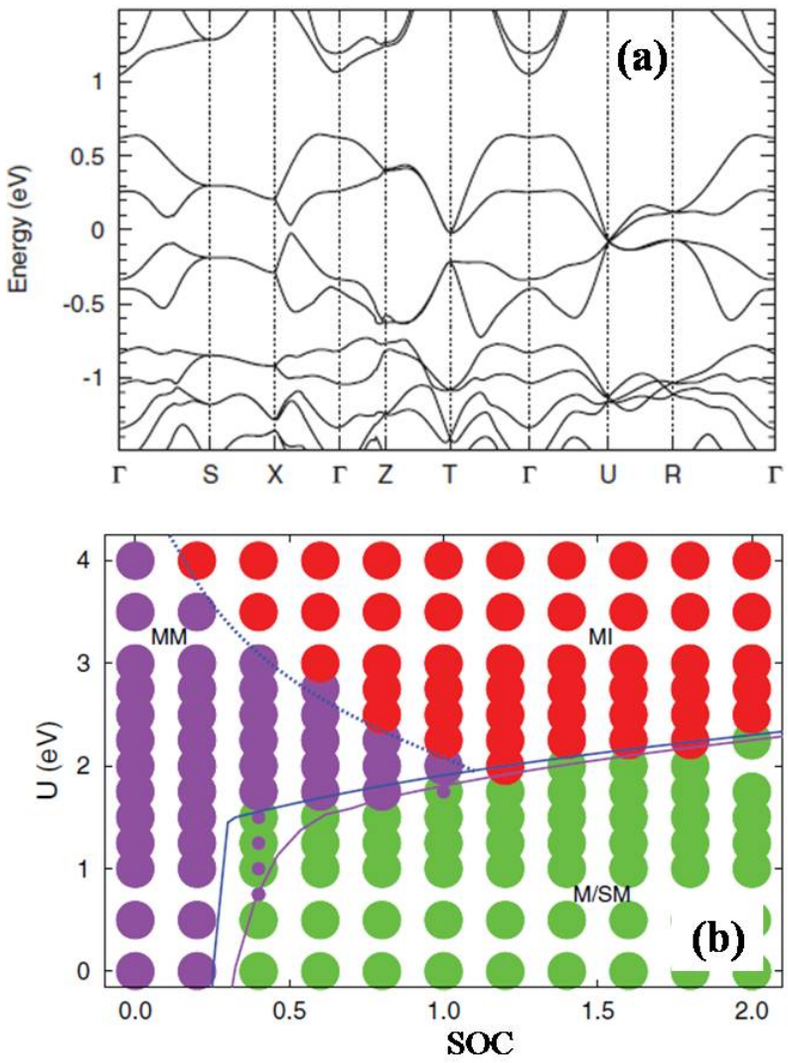

Figure 8. (a) LDA band structure of Pv $SrIrO_3$ with Hubbard U = 2 eV and SOC, demonstrating the presence of the node near the U point of J_{eff} = 1/2 band near the Fermi level; (b) the phase diagram of Pv $SrIrO_3$ in the U-SOC plane containing three phases: magnetic metal (MM), nonmangetic metal or semimetal (M/SM), and magnetic insulator (MI). Adapted from Reference [41].

of Pv $SrIrO_3$ to an antiferromagnetic insulator with a concomitant metal–insulator transition at T_N [50]. These recent experimental efforts demonstrated that semimetallic Pv $SrIrO_3$ is a promising candidate for realizing distinct topological and magnetic insulating states that deserve further investigations in the near future. On the other hand, the Pv $SrIrO_3$ film has also been regarded as potential electrode material for microelectronic devices [9].

4. $BaIrO_3$

At ambient pressure, $BaIrO_3$ crystallizes in the nine-layer (9R) polytype. It is the first known ferromagnetic insulator with $T_c \approx 180$ K among the 5d TMOs [17]. Detailed studies on single

crystals revealed a charge-density-wave (CDW) formation below the ferromagnetic order [18, 51]. Recent experimental [52] and theoretical [53] investigations further revealed it as an exotic spin-orbit Mott insulator that is of great current research interest. Following the general trend of perovskite hexagonal polytypes, we have explored the high-pressure sequences of $BaIrO_3$ and found three more polytypes, i.e. 5H, 6H, and 3C [19, 20, 21]. Their ground states exhibit an interesting evolution from a ferromagnetic insulator to a Pauli paramagnetic metal passing through a ferromagnetic quantum critical point tuned by the gradual structural changes as detailed below.

4.1. Synthesis

The ambient-pressure 9R phase can be readily obtained by sintering the stoichiometric mixtures of $BaCO_3$ and Ir at 1,000°C in air. The sample should be cooled down slowly for the last sintering in order to ensure an oxygen stoichiometry [54]. Single crystals have been reported to grow out of the $BaCl_2$ flux at a relatively low temperature of 1,000 K [18]. HPHT synthesis is needed for all the other polytypes [19, 21, 55, 56]. For the HP syntheses around 1,000°C, the 9R polytype is stable up to 3 GPa, the 5H phase exists only in a narrow pressure range around 4 GPa, the 6H phase is stabilized in a wide pressure range from 5 to ~20 GPa, and the 3C phase was finally obtained at 25 GPa. We have employed the two-stage (Walker- or Kawai-type) multianvil systems for the HPHT syntheses. During the HPHT experiments, the sample was first compressed to the desired pressure by eight truncated tungsten carbide anvils, and then the temperature was increased to ~1,000°C and kept for 30 min before quenching to room temperature. The resultant samples were recovered after releasing pressure and then subjected to various characterizations at ambient pressure.

4.2. Crystal structure

9R $BaIrO_3$ As shown in Figure 9(a), the crystal structure of the 9R phase consists of Ir_3O_{12} trimers of face-sharing octahedra that are linked by their vertices to form columns parallel to the *c*-axis, with a stacking of layers of corner-sharing (C) and face-sharing (F) IrO_6 octahedra in the order FFCFFCFFC along the *c* axis. Except for the monoclinic distortion, it is isostructural with the 9R $BaRuO_3$. The monoclinic distortion generates twisting and buckling of the Ir_3O_{12} trimers that are tilted ~12° relative to each other. Here, we adopted the crystal structure of 9R $BaIrO_{2.94}$ obtained by Powell et al. [54] from the NPD data, which were refined in a structural model defined in the *C2/m* space group, with three kinds of Ba atoms at 4*i* (*x*, 0, *z*) positions, four types of unequivalent Ir atoms at 4*i*, 2*a* (0, 0, 0) and 2*d* (0.5, 0, 0.5) sites, and six types of oxygen atoms at 4*i* and 8*j* (*x*, *y*, *z*) positions. The obtained unit-cell parameters are a = 9.9992 Å, b = 5.7490 Å, c = 15.1707 Å, and β = 103.27°. The final positional parameters and the selected bond lengths and bong angles after Reference [54] are listed in Table 6. Ir1–Ir2 and Ir3–Ir4 distances, of 2.618 Å and 2.627 Å respectively, are even smaller than the separation of 2.72 Å found in Ir metal, which indicates significant interactions between iridium cations at the centre of face-shared pairs of octahedra. It is important to note that, although this polytype has been compared to the ambient 9R $BaRuO_3$, with rhombohedral (*R-3m*) symmetry and a stacking

http://dx.doi.org/10.5772/61281

sequence $(FFC)_3$, the monoclinic distortion described for ambient 9R $BaIrO_3$ actually involves a shorter periodicity, with a stacking sequence $(FFC)_2$ along the *c* axis, as shown in Figure 9(a).

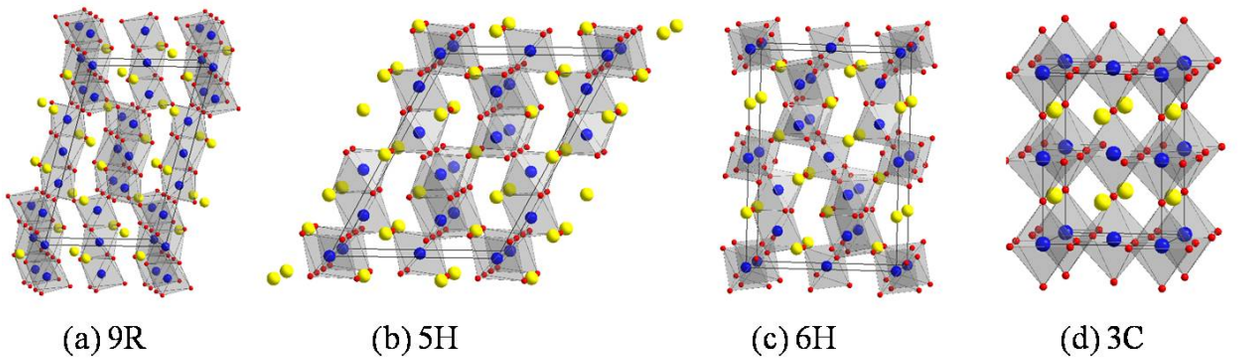

Figure 9. Crystal structure of the $BaIrO_3$ polytypes: (a) 9R, (b) 5H, (c) 6H, and (d) 3C.

Atom	Site	*x*	*y*	*z*	B_{iso} (Å^2)
Ba1	4i	0.7779	0	0.2501	0.42
Ba2	4i	0.3686	0	0.0720	0.42
Ba3	4i	0.1515	0	0.4224	0.42
Ir1	4i	0.0845	0	0.1766	0.16
Ir2	2a	0	0	0	0.16
Ir3	4i	0.4657	0	0.3230	0.16
Ir4	2d	0.5	0	0.5	0.33
O1	4i	0.2926	0	0.2287	0.33
O2	8j	0.0507	0.2421	0.2617	0.33
O3	4i	0.8931	0	0.0994	0.33
O4	8j	0.1164	0.2362	0.0839	0.33
O5	8j	0.4036	0.2291	0.4040	0.33
O6	4i	0.6427	0	0.4240	0.33

Ir1-O1	2.049	Ir1-Ir2	2.618
Ir1-O2 (×2)	1.979	Ir3-Ir4	2.627
Ir1-O3	2.001		
Ir1-O4 (×2)	2.032	Ir1-O1-Ir3	157.3
<Ir1-O>	2.01	Ir1-O2-Ir3	164.0
Ir2-O3 (×2)	2.038	Ir1-O3-Ir2	80.8

Atom	Site	*x*	*y*	*z*	B_{iso} (Å^2)
Ir2-O4 (×4)		2.034	Ir1-O4-Ir2		80.1
<Ir2-O>		2.04	Ir3-O5-Ir4		81.4
Ir3-O1		1.978	Ir3-O6-Ir4		80.0
Ir3-O2 (×2)		2.037			
Ir3-O5 (×2)		1.955			
Ir3-O6		2.057			
<Ir3-O>		2.02			
Ir4-O6 (×2)		2.030			
Ir4-O5 (×4)		2.035			
<Ir4-O>		2.03			

Table 6. Refined positional parameters and selected bond lengths (Å) and bond angles (°) for 9R $BaIrO_3$ from neutron diffraction [54]: space group *C2/m* (No. 12), *a* = 9.9992 Å, *b* = 5.7490 Å, *c* = 15.1707 Å, *β* = 103.27°, *V* = 848.81 Å^3, Z = 12.

5H $BaIrO_3$ The 5H phase was discovered as a new perovskite polytype [19]. As shown in Figure 9(b), its crystal structure contains chains of double dimer units that are corner-connected via oxygen atoms. These clusters of four octahedra are interleaved with single layers of vertex-sharing IrO_6 octahedra, forming infinite chains along the *c* axis. Adjacent chains are interlinked along the *a* and *b* directions via Ir–O–Ir vertex-sharing bridges. Alternatively, the structure can be described as stacking of layers of corner-sharing (C) and face-sharing (F) IrO_6 octahedra along the sequence FCFCC. The crystal structure was refined in the monoclinic *C2/m* (No. 12) space group, with three kinds of Ba atoms at 2*c* (0.5, 0.5, 0.5) and 4*i* (*x*, 0, *z*), three types of Ir atoms at 2*a* (0, 0, 0) and 4*i* sites, and six unequivalent oxygen atoms at 8*j* (*x*, *y*, *z*), 4*i*, 2*d* (0.5, 0, 0.5), and 4*f* (0.75, 0.75, 0) positions. The lattice parameters at room temperature are determined as *a* = 9.9554 Å, *b* = 5.7434 Å, *c* = 13.8049 Å, and *β* = 119.23°. The final positional parameters and the selected bond lengths and bond angles after Reference [19] are listed in Table 7. As can be seen, Ir–O distances vary in the range 1.90 Å for Ir1–O4 to 2.23 Å for Ir2–O3. The average value, of 2.03 Å, is consistent with the ionic radii sum for Ir^{4+} and O^{2-}. It is noteworthy that the structure contains three kinds of octahedra with rather distinct average sizes: <Ir–O> are 1.985 Å, 2.072 Å, and 2.017 Å for Ir1, Ir2, and Ir3 octahedra. The two largest octahedra, Ir2 and Ir3, are those forming dimers, where the Ir–O bonds are weakened by the Ir–Ir bonds. According to these bond distances, the bond valences for the three types of octahedra are 4.26(8)+, 3.35(8)+, and 4.06(9)+, indicating that Ir1 and Ir2 are under certain compressive and tensile stresses, respectively.

6H $BaIrO_3$ Same as the 6H $SrIrO_3$, the crystal structure of 6H $BaIrO_3$ consists of dimers of face-sharing octahedra separated by single corner-sharing octahedron, showing the sequence FCCFCC along the *c* axis. Based on the XRD data, we have refined its crystal structure in the monoclinic *C2/c* space group with two kinds of Ba atoms at 4*e* (0, *y*, ¼) and 8*f* (*x*, *y*, *z*) positions, Ir1 at 4*a* (0, 0, 0) and Ir2 at 8*f* sites, and four independent oxygen atoms, O1 at 4*e*, O2, O3, and O4 at 8*f* positions. The obtained unit-cell parameters are *a* = 5.7483 Å, *b* = 9.9390 Å, *c* = 14.3582

http://dx.doi.org/10.5772/61281

Å, and $\beta = 91.319°$. The final positional parameters and selected bond lengths and bond angles after Reference [19] are listed in Table 8. As can be seen, the $Ir2O_6$ octahedra within the face-sharing dimmers are considerably more expanded than the $Ir1O_6$ octahedra, with average Ir–O distances of 2.16 and 1.99 Å, respectively. This is probably a consequence of the metal–metal bond linking the couples of Ir2 atoms in the dimmers, with Ir2–Ir2 distances of 2.710 Å.

Atom	Site	*x*	*y*	*z*	B_{iso} (Å^2)
Ba1	2c	0.5	0.5	0.5	1.2
Ba2	4i	-0.191	0	0.7139	0.1
Ba3	4i	-0.247	0.5	0.8886	0.9
Ir1	2a	0	0	0	3.2
Ir2	4i	-0.4529	0	0.8215	1.0
Ir3	4i	-0.6046	0	0.5920	2.4
O1	8j	0.053	0.72	0.7002	2.3
O2	8j	-0.0093	-0.770	0.1085	1.2
O3	4i	0.703	0	0.303	4.0
O4	4i	0.217	0	0.0607	0.6
O5	2d	0.5	0	0.5	1.5
O6	4f	0.75	0.75	0.5	3.9
Ir1-O2 (×4)	2.029	Ir2-Ir3	2.735		
Ir1-O4 (×2)	1.898				
<Ir1-O>	1.985	Ir2-O1-Ir3	84.0		
Ir2-O1 (×2)	2.12	Ir1-O2-Ir2	165.1		
Ir2-O2 (×2)	2.23	Ir2-O3-Ir3	79.1		
Ir2-O3	2.038	Ir1-O4-Ir2	160.3		
Ir2-O4	2.105	Ir3-O5-Ir3	180		
<Ir2-O>	2.072	Ir3-O6-Ir3	180		
Ir3-O1 (×2)	2.004				
Ir3-O3	2.11				
Ir3-O5	1.994				
<Ir3-O>	2.017				

Table 7. Refined positional parameters and selected bond lengths (Å) and bond angles (°) for 5H $BaIrO_3$ from neutron diffraction [19]: space group *C2/m* (No. 12), $a = 9.9554$ Å, $b = 5.7434$ Å, $c = 13.8049$ Å, $\beta = 119.231°$, $V = 688.8$ Å^3, $Z = 10$.

3C $BaIrO_3$ A single-phase Pv $BaIrO_3$ was finally obtained at 25 GPa [21]. Instead of the simple cubic phase with space group *Pm-3m*, it was found that the XRD pattern of the Pv phase can

be refined excellently in the tetragonal *I*4/*mcm* (No. 140) space group with the Ba atom at *4b* (0, ½, ¼), the Ir atom at *4c* (0, 0, 0), and two kinds of O atoms at *4a* (0, 0, ¼) and *8h* (*x*, *x*+½, 0) sites. The obtained unit-cell parameters are $a = b = 5.7044$ Å and $c = 8.0926$ Å. The final positional parameters and the main bond distances and bond angles after Reference [21] are listed in Table 9. It should be noted that we denoted this phase as "3C" in order to follow the conventional notations.

Atom	Site	*x*	*y*	*z*	B_{iso} (Å²)
Ba1	4e	0	-0.0052	1/4	0.3
Ba2	8f	0.0078	0.3349	0.0912	0.25
Ir1	4a	0	0	0	0.4
Ir2	8f	0.9936	0.3323	0.8442	0.27
O1	4e	0	0.499	1/4	-0.2
O2	8f	0.2180	0.2390	0.2427	-0.2
O3	8f	0.036	0.846	0.0852	-0.2
O4	8f	0.286	0.087	0.049	-0.2
O5	8f	0.809	0.090	0.103	-0.2
Ir1-O3 (×2)	1.93	Ir1-O3-Ir2	164.4		
Ir1-O4 (×2)	2.02	Ir1-O4-Ir2	151.4		
Ir1-O5 (×2)	2.01	Ir1-O5-Ir2	153.6		
<Ir1-O>	1.99				
Ir2-O1	2.19	Ir2-O1-Ir2	76.4		
Ir2-O2	2.22	Ir2-O1-Ir2	75.1		
Ir2-O2	2.23				
Ir2-O3	2.10				
Ir2-O4	2.09				
Ir2-O5	2.11				
<Ir2-O>	2.16				
Ir2-Ir2	2.710				

Table 8. Refined positional parameters and selected bond lengths (Å) and bond angles (°) for 6H $BaIrO_3$ from powder XRD [19]: space group *C*2/*c* (No. 15), $a = 5.7483$ Å, $b = 9.9390$ Å, $c = 14.3582$ Å, $\beta = 91.319°$, $V = 820.12$ Å³, Z = 12.

The small tetragonal distortion of the 3C $BaIrO_3$ phase is unexpected; we should have a cubic phase as found for $BaRuO_3$ formed under high pressure. Such a distortion to tetragonal symmetry by cooperative rotations of the $IrO_{6/2}$ octahedra about the *c* axis is typical of an $A^{2+}B^{4+}O_3$ perovskite with a tolerance factor $t \equiv (A-O)/[\sqrt{2}\ (B-O)]$ a little smaller than unity. However, stabilization of $BaIrO_3$ in the 9R polytype at ambient pressure is consistent with $t > 1$ obtained from tabulated equilibrium ionic radii. The larger compressibility of the Ba–O bond

http://dx.doi.org/10.5772/61281

makes it possible to stabilize the 3C phase of $BaIrO_3$ under 25 GPa pressure, but compression of the Ba–O bond by cubic symmetry should not reduce the tolerance factor below $t = 1$. Retention of the cubic symmetry of the IrO_6 octahedra shows that the threefold degeneracy of the 5d π^* bands is not a factor. In fact, the tolerance factor calculated from the measured <Ba–O> and <Ir–O> bond lengths in Table 9 gives a $t = 0.998$ consistent with the tetragonal structure observed. Therefore, we conclude that at 25 GPa there has been a first-order transition of the Ba–O equilibrium bond length to give a $t < 1$, which indicates that the 5d π^* bands of the IrO_6 array may also have transitioned for J_{eff} =1/2 and 3/2 bands as a result of a reduction of the orbital angular momentum where the bandwidth is broadened. The high-pressure equilibrium (Ba–O) bond length is retained as a metastable bond length on removal of the pressure, and the Ir–O bonds are not under a tensile stress.

Atom	Site	*x*	*y*	*z*	B_{iso} (Å²)
Ba	4b	0	0.5	1/4	0.72
Ir	4c	0	0	0	0.49
O1	4a	0	0	1/4	0.8
O2	8h	0.2313	0.7313	0	0.8
Ir-O1 (×2)	2.023		Ir-O1-Ir	180	
Ir-O2 (×2)	2.023		Ir-O2-Ir	171.1	
<Ir-O>	2.023				

Table 9. Refined positional parameters and selected bond lengths (Å) and bond angles (°) for 3C $BaIrO_3$ from powder XRD [21]: space group *I4/mcm* (No. 140), $a = b = 5.7044$ Å, $c = 8.0916$ Å, $V = 263.30$ Å^3, Z = 4.

Polytype structures The polytype structures of the ABO_3 oxides and the phase transformation under high pressure were established during the 1960–1970s, see the Review [57]. As a general trend, the number of the hexagonal close packing along the *c* axis in a unit cell is reduced as the synthesis pressure increases, which led to a decrease (increase) of face(corner)-sharing octahedra. This is consistent with that fact that pressure stabilizes preferentially the denser phase. The observed crystallographic densities of the 9R, 5H, 6H and 3C phases of $BaIrO_3$ are 8.84, 9.08, 9.17, and 9.36 g/cm^3, respectively. They progressively increase as expected, since these phases have been stabilized at increasing pressures. This sequence corresponds, therefore, to more dense packing of the BaO_3 layers along the *c* axis, showing an evolution to structures with more corner (C) sharing and fewer face (F) sharing octahedra, i.e. C:F ratios increase in the order 1:2 (9R), 3:2 (5H), 2:1 (6H), and ∞ (3C). As detailed below, the physical properties exhibit interesting evolution in response to these systematic structural variations.

4.3. Physical properties

9R $BaIrO_3$ As mentioned above, 9R $BaIrO_3$ is the first known ferromagnet among the 5d TMOs [17]. Cao et al. [18] performed the first detailed experimental study on the single-crystal samples and uncovered a CDW formation accompanying the ferromagnetic order at $T_c \approx 180$

K. The experimental evidences in support of the CDW formation included [18]: (1) a sudden increase of resistivity at T_c, (2) the presence of non-linear conductivity with negative differential resistivity below T_c, (3) an optical gap formation at ~ 1,200 $cm^{-1} \approx 9\kappa_B T_c$ in the electron excitation spectrum and a splitting of a phonon mode at 350 cm^{-1} for $T < T_c$, and (4) the emergent X-ray satellite structure below T_c. Besides the transitions at $T_c \approx 180$ K, two additional anomalies have also been observed [18] upon cooling on the c-axis resistivity ρ_c, which first changes to a metallic behaviour below $T_1 = 80$ K and then suddenly enters a Mott-like insulating state below $T_2 = 26$ K, Figure 10. These two additional transitions are absent for the resistivity within the *ab* plane. The simultaneous occurrence of ferromagnetic order and CDW formation is quite unusual, and 9R $BaIrO_3$ has thus been the subject of extensive investigations since then. Later on, Nakano and Terasaki [51] carried out similar current-voltage (I-V) measurements on their single crystals by using a pulsed current in order to exclude the self-heating effects. Their observations of the giant nonlinear conduction only appearing below 30 K, well below $T_c \approx$ 180K, questioned the above scenario of a simultaneous onset of a CDW and a ferromagnetic transition. Instead of the sliding motion of CDW, they proposed an interplay between two different bands is likely the origin of the nonlinear conduction observed in $BaIrO_3$ [51]. Such discrepancy might arise from the different sample quality. Nevertheless, a clear gap opening is unambiguously evidenced at T_c by other experimental probes, such as the Seebeck coefficient [51, 58] and the high-resolution photoemission spectroscopy [59]. Currently, it remains elusive whether the gap opening is driven by the magnetic order or the Fermi surface nesting.

The observation of weak ferromagnetism and insulating ground state in the 9R $BaIrO_3$ has attracted renewed interest in recent years in light of the SOC-driven Mott insulating state for iridates. As for the nature of the weak ferromagnetism, there also exist long-standing discrepancies. Experimentally, a tiny Ir moment of ~0.03 μ_B/Ir was observed below T_c. In addition, a modified Curie-Weiss fitting to the inverse susceptibility also evidenced a small effective moment of ~ 0.13 μ_B [18]. Originally, a spin canting from a localized full-moment antiferromagnetic configuration had been invoked to explain the tiny ordered moment [17]. In contrast, Cao et al. [18] proposed a model of band magnetism with intrinsically small Ir moment due to d–p hybridization and small exchange splitting. Indeed, the muon-spin relaxation measurements by Brooks et al. [60] provided direct experimental evidences in support of a small Ir moment, i.e. they observed clear oscillations below T_c and found an extremely small internal field at the muon site. Such an itinerant picture of band magnetism, however, is incompatible with the observation of high coercive force and anisotropy in magnetization measurements. By employing the X-ray absorption spectroscopy (XAS) and X-ray magnetic circular dichroism (XMCD) techniques, Laguna-Marco et al. [52] recently elucidated an atomic-like nature of the Ir moment with the orbital moment being ~1.5 times larger than the spin moment, thus highlighting the importance of SOC in addressing the magnetic order of 9R $BaIrO_3$. After taking into account both SOC and moderate on-site coulomb interactions, first-principles calculations by Ju et al. [53] identified 9R $BaIrO_3$ as an exotic spin-orbit Mott insulator with multiple J_{eff} = 1/2 states associated with the unique face-sharing Ir_3O_{12} octahedral units within the structure.

Although the atomic-like nature of Ir local moment in 9R $BaIrO_3$ was found to be extremely stable against temperature, pressure, and chemical substitutions [52, 61], these external stimuli

http://dx.doi.org/10.5772/61281

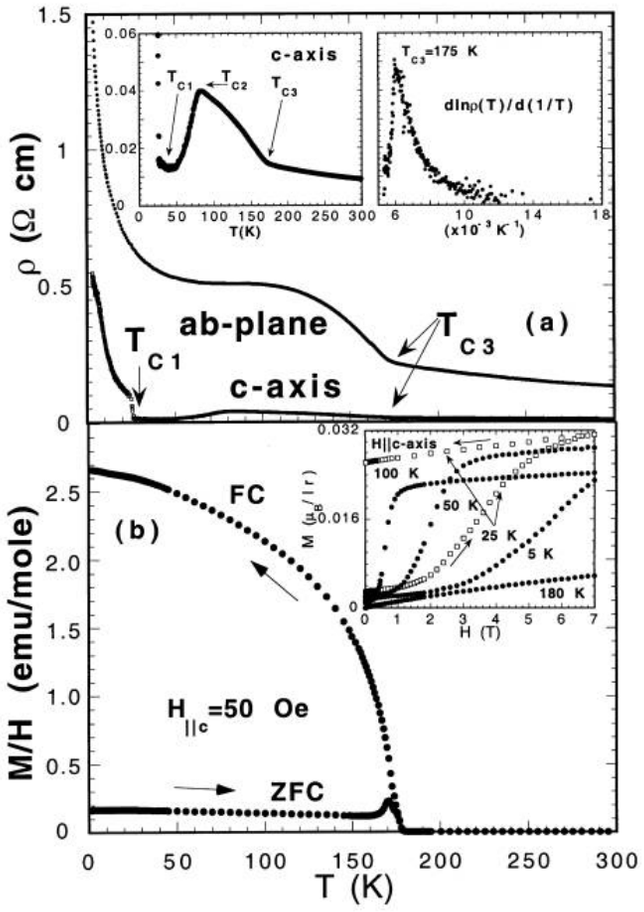

Figure 10. (a) Temperature dependence of resistivity for 9R $BaIrO_3$ for two major crystallographic directions. The first inset shows details of c-axis conductivity and the second the sharp peak in dlnρ/d(1/*T*) denotes the onset of ferromagnetism. (b) Field-cooled (FC) ad zero field-cooled (ZFC) magnetization showing the ferromagnetic transition at T_c. The inset shows isothermal magnetization at several temperatures, illustrating a large hysteresis. Adapted from Reference [18].

can easily lead to a breakdown of the weak ferromagnetism and nonmetallic ground state. For example, Cao et al. [62] grown a series of Sr-doped $Ba_{1-x}Sr_xIrO_3$ single crystals and found that the chemical pressure applied via Sr doping drastically suppresses T_c and immediately leads to a non-metal to metal transition at high temperatures. On the other hand, although the application of external pressure of ~4.5 GPa can also quench the weak ferromagnetism as Sr doping, $BaIrO_3$ becomes more insulating under pressure [61]. Such a disparate response of transport and magnetic properties to the chemical and physical pressure has been ascribed to the different compression rates of the lattice parameters *a* and *c* upon Sr doping and external pressure. Interestingly, Korneta et al. [63] found that a dilute rare-earth R^{3+} doping (~ 4%) of $BaIrO_3$ can also suppress the weak ferromagnetism and lead to a metallic state, whereas the application of modest external pressure readily restores the insulating state. Further studies are needed to clarify whether the weak ferromagnetism is also recovered in the pressure-induced insulating state. All these above results demonstrate a delicate interplay between structural and electronic degrees of freedom in 9R $BaIrO_3$.

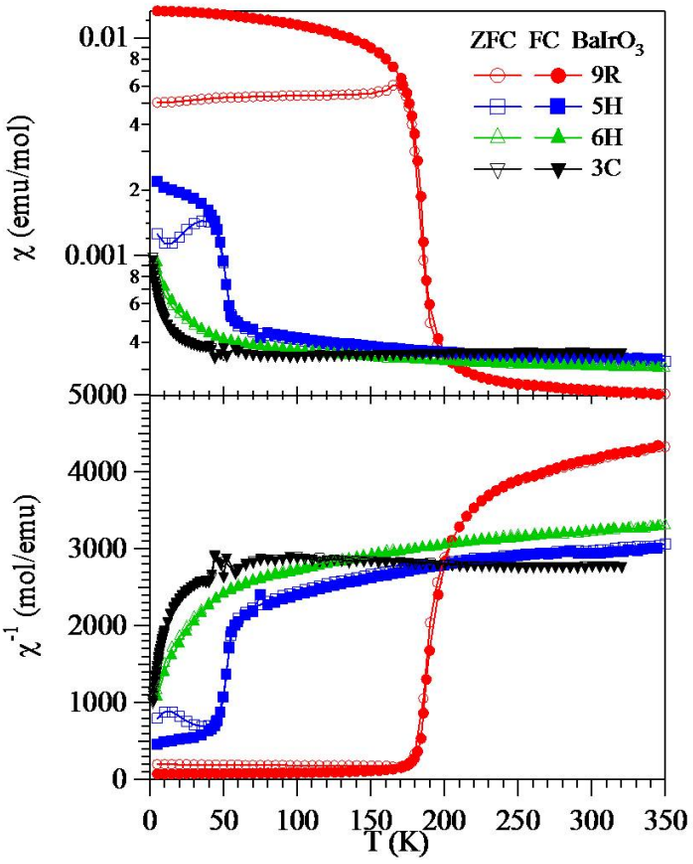

Figure 11. Temperature dependence of magnetic susceptibility $\chi(T)$ and its inverse $\chi^{-1}(T)$ for the $BaIrO_3$ polytypes, illustrating the evolution of the magnetic ground state. Adapted from Reference [21].

5H $BaIrO_3$ The 5H phase is a weak ferromagnetic metal with $T_c \approx 50$ K, Figure 11. Cheng et al. [20] and Zhao et al. [56] have characterized this compound through measurements of magnetic susceptibility $\chi(T)$, resistivity $\varrho(T)$, thermoelectric power S(T), and specific heat C(T). A weak ferromagnetic transition at $T_c \approx 50$ K was clearly observed in $\chi(T)$, and well reflected as a kink in the plots of ρ vs T, S/T vs ln$T$, and C/T vs T. *In situ* high-pressure resistivity measurements show that T_c decreases gradually with pressure, and reaches about 40 K under 1.5 GPa.

6H $BaIrO_3$ The 6H phase has been independently identified and characterized by Zhao et al. [55] and Cheng et al. [20]. Similar with the 6H $SrIrO_3$, it is an exchange-enhanced paramagnetic metal with non-Fermi-liquid behaviours. Zhao et al. [55] reported that its resistivity $\rho(T)$ follows a linear T dependence below 20 K, whereas a $T^{5/3}$ dependence was observed for $T < 60$ K by Cheng et al. [20]. Such a discrepancy should arise from the polycrystalline nature of the studied samples. As mentioned above, a non-Fermi-liquid $\rho \sim T^{3/2}$ behaviour has also been found in the 6H $SrIrO_3$ single crystals due to the proximity to a ferromagnetic quantum critical point. In order to verify similar situation taking place in 6H $BaIrO_3$, we measured the thermopower $S(T)$ that is insensitive to grain boundaries. We indeed found a linear relationship in the plot of S/T versus $-\ln T$ over a wide temperature range, in strong support of the realization of ferromagnetic quantum critical point [20]. Based on the low-temperature specific heat and

http://dx.doi.org/10.5772/61281

magnetic susceptibility, the obtained Sommerfeld–Wilson ratio $R_W = \frac{\pi^2}{3}\left(\frac{k_B}{\mu_B}\right)^2 \frac{\chi_0}{\gamma} = 2.14(3)$ provides further evidence for strong electron-electron correlations.

3C $BaIrO_3$ 3C $BaIrO_3$ is characterized as a Pauli paramagnetic metal with a Fermi-liquid behaviour [21]. Its resistivity $\rho(T)$ displays a metallic behaviour down to at least 1.8 K and follows the Fermi-liquid behaviour, i.e. $\rho(T) = \rho_0 + AT^2$ below 6 K with $\rho_0 = 0.0584(1)$ Ω cm and $A = 8.1(1)$ μΩ cm K^{-2}, respectively. The magnetic susceptibility $\chi(T)$ exhibits a nearly temperature-independent Pauli paramagnetism with a shallow minimum around 85 K as observed around $T^* \approx 170$ K in Pv $SrIrO_3$. Such an upturn with temperature has been ascribed to the higher-order temperature-dependent term in the Pauli paramagnetism. Low-temperature specific heat C(T) analysis yields an electronic specific-heat coefficient $\gamma = 6.84(6)$ mJ/mol K^2 and a Debye temperature $\Theta_D = 335$ K.

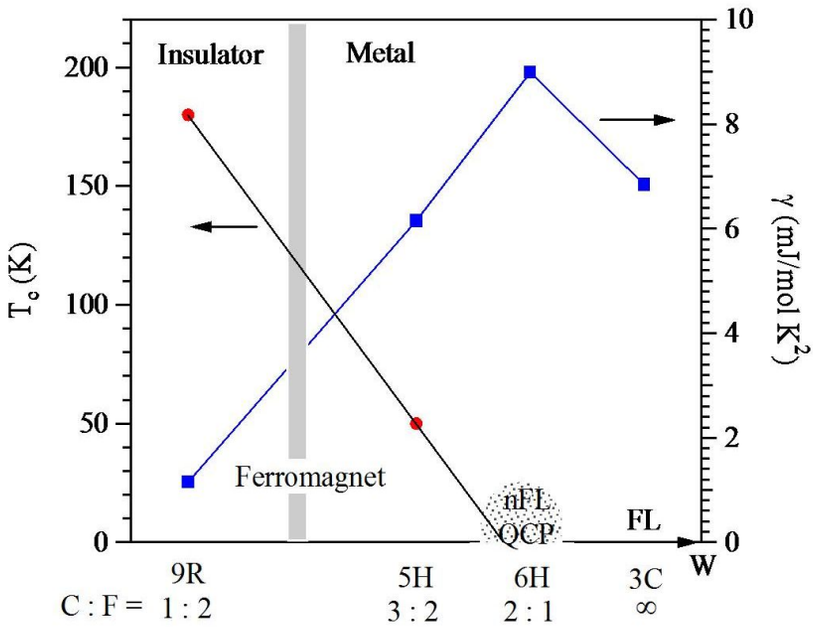

Figure 12. A schematic phase diagram of the $BaIrO_3$ polytypes showing the evolution of magnetic transition temperautre T_c (left) and the electronic specific-heat coeffcieint γ (right) as a function of the corner-to-face sharing octahedral C:F ratio. Adapted from Reference [21].

Structure–property evolutions in the $BaIrO_3$ polytypes As shown in Figure 9, the major change of the crystal structures for these polytypes can be described by the stacking sequence of IrO_6 octahedra that evolves from 9R(CFFCFFCFF) → 5H(CFCCF) → 6H(CCFCCF) → 3C(CCC), where C and F stands for corner- and face-sharing, respectively. Figure 11 displays the temperature dependence of magnetic susceptibility $\chi(T)$ and its inverse $\chi^{-1}(T)$ for the $BaIrO_3$ polytypes, illustrating the evolution of the magnetic ground state. Figure 12 shows a schematic phase diagram of the $BaIrO_3$ polytypes. With increasing C:F ratio in the sequence 9R(1:2) → 5H(3:2) → 6H(2:1) → 3C(∞), the ground states of $BaIrO_3$ evolve from a ferromagnetic insulator with $T_c = 180$ K in the 9R phase to a ferromagnetic metal with $T_c = 50$ K in the 5H phase, then to an exchange-enhanced paramagnetic metal with non-Fermi-liquid behaviour near a

ferromagnetic quantum critical point in the 6H phase, and finally to a Fermi-liquid metal in the 3C phase. Such a structure–physical property evolution has been ascribed to a progressive bandwidth broadening in the sense that the corner-shared arrangement of IrO_6 octahedron can facilitate the Ir overlap integral mediated via O-2p orbitals. Since the electronic specific-heat coefficient γ is proportional to the density of states at the Fermi energy, the gradual enhancement of γ from 9R to 6H phase shown in Figure 12 is in agreement with the bandwidth argument. Both the 6H and 3C phases are metallic. Since the 6H phase is close to a ferromagnetic quantum critical point, the γ is much enhanced due to critical fluctuations relative to that in the 3C phase with an even broader bandwidth. From this systematic study on $BaIrO_3$ polytypes, we can understand why the 6H $SrIrO_3$ is a non-Fermi-liquid metal near a ferromagnetic quantum critical point [11]. Moreover, the study on $BaIrO_3$ demonstrated that HPHT synthesis of structurally closely related perovskite polytypes represents an effective approach to fine tune the physical properties of interest via modifying the octahedral arrangement.

5. Conclusions

We have summarized in this chapter the current knowledge on the materials' synthesis, crystal structure, and physical properties of the "113" alkaline-earth iridates $AIrO_3$ (A = Ca, Sr, Ba), which display a rich variety of crystallographic and electronic states that are of great current research interest. For $CaIrO_3$, it can form in either the layered pPv or the orthorhombic Pv structure, and thus serves as an important analogue of $MgSiO_3$ to investigate the Pv/pPv transformation in the Earth's lowermost mantle in geosciences. Corresponding to different crystal structures, their electronic ground states differ sharply: the pPv phase is an antiferromagnetic Mott insulator with T_N = 110 K while the Pv phase is a paramagnetic semimetal with possible Dirac nodes protected by the lattice symmetry. The presence of strong structural distortion in pPv $CaIrO_3$ makes it a model system to investigate the interplay of non-cubic crystal field and SOC in iridates. On the other hand, metallization of the pPv phase via electron or hole doping represents an important approach to realize the exotic electronic states on the verge of insulator–metal transition. For $SrIrO_3$, it crystallizes in the 6H polytype at ambient pressure and transforms to the orthorhombic Pv structure under high-pressure conditions. The 6H phase is an exchange enhanced paramagnetic metal with non-Fermi-liquid behaviour due to the proximity of ferromagnetic quantum critical point, while the Pv phase is revealed as an exotic narrow-band semimetal with symmetry-protected Dirac nodes within the J_{eff} = 1/2 band near the Fermi level. The presence of nontrivial features in the low energy electronic states makes these "113" orthorhombic Pv iridates $AIrO_3$ (A = Ca, Sr) promising candidates for realizing various topological and magnetic insulating phases via tuning the SOC, Hubbard interactions, and/or lattice symmetry. In this regard, epitaxial growth of superlattices and high-pressure synthesis of bulk materials with proper chemical design are currently important approaches to tailor the proposed quantum phases out of the semimetallic state. For $BaIrO_3$, it adopts a nine-layer 9R polytype at ambient pressure, and can be transformed to 5H, 6H, and 3C phases under different high pressure conditions. The 9R phase is a weak ferromagnetic insulator with T_c = 180 K, and can be regarded as an exotic SOC Mott insulator with multiple J_{eff} = 1/2 states associated with the unique Ir_3O_{12} structural units. An atomic-like nature of the

http://dx.doi.org/10.5772/61281

Ir moment driven by strong SOC is rather stable against external perturbations, but the weak ferromagnetism can be easily suppressed by applying chemical and physical pressures or dilute rare-earth substitutions for Ba^{2+}. In contrast, the nonmetallic ground state displays distinct response to the chemical and physical pressure, highlighting the delicate interplay of crystal structure and electronic degrees of freedom for this quasi-1D compound. With increasing the ratio of corner-to-face sharing octahedra in the sequence 9R(1:2) → 5H(3:2) → 6H(2:1) → 3C(∞), the ground states of $BaIrO_3$ evolve from a ferromagnetic insulator with T_c = 180 K in the 9R phase to a ferromagnetic metal with T_c = 50 K in the 5H phase, then to an exchange-enhanced paramagnetic metal with non-Fermi-liquid behaviour near a ferromagnetic quantum critical point in the 6H phase, and finally to a Fermi-liquid metal in the 3C phase. Such a structure–physical property evolution demonstrated that HPHT synthesis of structurally closely related perovskite polytypes represents an effective approach to fine tune the physical properties of interest via modifying the octahedral arrangement.

Acknowledgements

We are grateful to J.-Z. Zhou, J. B. Goodenough, José Alonso, Y. Uwatoko, and M. Akaogi for collaborations on work related to this review. This work is supported by the National Basic Research Program of China (Grant No. 2014CB921500), the National Science Foundation of China (Grant Nos. 11304371, 51402019), and the strategic Priority Research Program of the Chinese Academy of Sciences (Grant No. XDB07020100).

Author details

Yunqi Cai[1], Yan Li[2] and Jinguang Cheng[1*]

*Address all correspondence to: jgcheng@iphy.ac.cn

1 Beijing National Laboratory for Condensed Matter Physics and Institute of Physics, Chinese Academy of Sciences, Beijing, China

2 College of Materials Science and Engineering, Beijing Institute of Petrochemical Technology, Beijing, China

References

[1] Cao G, Bolivar J, McCall S, Crow JE, Guertin RP. Weak ferromagnetism, metal-to-nonmetal transition, and negative differential resistivity in single-crystal Sr_2IrO_4. Phys Rev B 1998;57:R11039.

[2] Kim BJ, Jin H, Moo SJ, Kim JY, Park BG, Leem CS, Yu J, Noh TW, Kim C, Oh SJ, Park JH, Durairaj V, Cao G, Rotenberg E. Novel J_{eff}=1/2 Mott state induced by relativistic spin-orbit coupling in Sr_2IrO_4. Phys Rev Lett 2008;101:076402.

[3] Kim BJ, Ohsumi H, Komesu T, Sakai F, Morita T, Takagi H, Arima T. Phase sensitive observation of a spin-orbital Mott state in Sr_2IrO_4. Science 2009;323:1329.

[4] Jackeli G, Khaliullin G. Mott insulators in the strong spin-orbit coupling limit: from Heisenberg to a quantum compass and Kitaev models. Phys Rev Lett 2009;102:017205.

[5] Witczak-Krempa W, Chen G, Kim YB, Balents L. Correlated quantum phenomena in the strong spin-orbit regime. Annu Rev Condens Matter Phys 2014;5:57–82.

[6] Cao G, Delong LE. Frontiers of 4d- and 5d-Transition Metal Oxides. World Scientific Publishing Co. Pte. Ltd.; 2013.

[7] Moon SJ, Jin H, Kim KW, Choi WS, Lee YS, Yu J, Cao G, Sumi A, Funakubo H, Bernhard C, Noh TW. Dimensionality-controlled insulator-metal transition and correlated metallic state in 5d transition metal oxides $Sr_{n+1}Ir_nO_{3n+1}$ (n = 1, 2, and infinite). Phys Rev Lett 2008;101:226402.

[8] Longo JM, Kafalas JA, Arnott RJ. Structure and properties of the high and low pressure forms of $SrIrO_3$. J Solid State Chem 1971;3:174–9.

[9] Kim YK, Sumi A, Takahashi K, Yokoyama S, Ito S, Watanabe T, Akiyama K, Kaneko S, Saito K, Funakubo H. Metalorganic chemical vapour deposition of epitaxial perovskite $SrIrO_3$ films on (100) $SrTiO_3$ substrates. J Appl Phys 2006;45:L36–8.

[10] Carter JM, Vijay Shankar V, Ahsan Zeb M, Kee HY. Semimetal and topological insulator in perovskite iridates. Phys Rev B 2012;85:115105.

[11] Cao G, Durairaj V, Chikara S, DeLong LE, Parkin S, Schlottmann P. Non-Fermi-liquid behaviour in nearly ferromagnetic $SrIrO_3$ single crystal. Phys Rev B 2007;76:100402(R).

[12] Sarkozy RF, Moeller CW, Chamberland BL. The characterization of calcium iridium oxides. J Solid State Chem 1974;9:242–6.

[13] Ohgushi K, Yagi T, Gotou H, Kiuchi Y, Ueda Y. Metallization of quasi-two-dimensional Mott insulator $CaIrO_3$ with S = 1/2 spins. Physica B 2009;404:3261–3.

[14] Ohgushi K, Yamaura J, Ohsumi H, Sugimoto K, Takeshita S, Tokuda A, Takagi H, Takata M, Arima T. Resonant X-ray diffraction study of the strongly spin-orbit-coupled Mott insulator $CaIrO_3$. Phys Rev Lett 2013;110:217212.

[15] Moretti Sala M, Ohgushi K, Al-Zein A, Hirata Y, Monaco G, Krisch M. $CaIrO_3$: a spin-orbit Mott insulator beyond the j_{eff}=1/2 ground state. Phys Rev Lett 2014;112:176402.

[16] Shim S-H. The postperovskite transition. Annu Rev Earth Planet Sci 2008;36:569.

[17] Lindsay R, Strange W, Chamberland BL, Moyer JR. Weak ferromagnetism in $BaIrO_3$. Solid State Comm 1993;86:759–63.

[18] Cao G, Crow JE, Guertin RP, Henning PF, Homes CC, Strongin M, Basov DN, Lochner E. Charge density wave formation accompanying ferromagnetic ordering in quasi-one-dimensional $BaIrO_3$. Solid State Comm 2000;113:657–62.

[19] Cheng JG, Alonso JA, Suard E, Zhou JS, Goodenough JB. A new perovskite polytype in the high-pressure sequence of $BaIrO_3$. J Am Chem Soc 2009;131:7461–9.

[20] Cheng JG, Zhou JS, Alonso JA, Goodenough JB, Sui Y, Matsubayashi K, Uwatoko Y. Transition from a weak ferromagnetic insulator to an exchange-enhanced paramagnetic metal in the $BaIrO_3$ polytypes. Phys Rev B 2009;80:104430.

[21] Cheng JG, Ishii T, Kojitani H, Matsubayashi K, Matsuo A, Li X, Shirako Y, Zhou JS, Goodenough JB, Jin CQ, Akaogi M, Uwatoko K. High-pressure synthesis of the $BaIrO_3$ perovskite: a Pauli paramagnetic metal with a Fermi liquid ground state. Phys Rev B 2013;88:205114.

[22] McDaniel CL, Schneider SJ. Phase relations in the CaO-IrO_2-Ir system in air. J Solid State Chem 1972;4:275–80.

[23] Rodi VF, Babel D. Erdalkaliiridium (IV) oxide: Kristallstruktru von $CaIrO_3$. Z. Anorg Allg Chem 1965;336:17–23.

[24] Oganov AR, Ono S. Theoretical and experimental evidence for a post-perovskite phase of $MgSiO_3$ in Earth's D'' layer. Nature 2004;430:445–8.

[25] Ohgushi K, Goto H, Yagi T, Kiuchi Y, Sakai F, Ueda Y. Metal-insulator transition in $Ca_{1-x}Na_xIrO_3$ with post-perovskite structure. Phys Rev B 2006;74:241104(R).

[26] Hirai D, Matsuno J, Takagi H. Semimetallic transport properties of epitaxially stabilized perovskite $CaIrO_3$ films. ArXiv:1501.01433. 2015.

[27] Hirai S, Sanehira T, Nishiyama N, Irifune T, Klemme S, Bromiley G, Attfield JP. Tunning of structure, morphology, and magnetism in postperovskite oxide solid solutions. Chem Mater 2011;23:114–21.

[28] Sugahara M, Yoshiasa A, Yoneda A, Hashimoto T, Sakai S, Okube M, Nakatsuka A, Ohtaka O. Single-crystal X-ray diffraction study of $CaIrO_3$. Am Miner 2008;93:1148–52.

[29] Hirai S, Welch MD, Aguado F, Redfern SAT. The crystal structure of $CaIrO_3$ post-perovskite revisited. Z Kristallogr 2009;224:345–50.

[30] Cheng JG, Zhou JS, Goodenough JB, Sui Y, Ren Y, Suchomel MR. High-pressure synthesis and physical properties of perovskite and post-perovskite $Ca_{1-x}Sr_xIrO_3$. Phys Rev B 2011;83:064401.

[31] Kojitani H, Furukawa A, Akaogi M. Thermochemistry and high-pressure equilibria of the post-perovskite phase transition in $CaIrO_3$. Am Miner 2007;92:229–32.

[32] Jang SY, Kim H, Moo SJ, Choi WS, Jeon BC, Yu J, Noh TW. The electronic structure of epitaxially stabilized 5d perovskite $Ca_{1-x}Sr_xIrO_3$ (x = 0, 0.5, and 1) thin films: the role of strong spin-orbit coupling. J Phys: Condens Matter 2010;22:485602.

[33] Subedi A. First-principles study of the electronic structure and magnetism of $CaIrO_3$. Phys Rev B 2012;85:020408(R).

[34] Bagdanov NA, Katukuri VM, Stoll H, Brink J, Hozoi L. Post-perovskite $CaIrO_3$: A j=1/2 quasi-one-dimensional antiferromagnet. Phys Rev B 2012;85:235147.

[35] Gunasekera J, Chen Y, Kremenak JW, Miceli PF, Singh DK. Mott insulator-to-metal transition in yttrium doped $CaIrO_3$. J Phys: Condens Matter 2015;27:052201.

[36] Kojitani H, Shirako Y, Akaogi M. Post-perovskite phase transition in $CaRuO_3$. Phys Earth Planet Inter 2007;165:127–34.

[37] Yamaura K, Shirako Y, Kojitani H, Arai M, Young DP, Akaogi M, Nakashima M, Katsumata T, Inaguma Y, Takayama-Muromachi E. Synthesis and magnetic and charge-transport properties of the correlated 4d post-perovskite $CaRhO_3$. J Am Chem Soc 2009;131:2722–6.

[38] Shirako Y, Satsukawa H, Wang XX, Li JJ, Guo YF, Arai M, Yamaura K, Yoshida M, Kojitani H, Katsumata T, Inaguma Y, Hiraki K, Takahashi T, Akaogi M. Integer spin-chain antiferromagnetism of the 4d oxide $CaRuO_3$ with post-perovskite structure. Phys Rev B 2011;83:174411.

[39] Zhong GH, Li YL, Liu Z, Zeng Z. Ground state properties of perovskite and post-perovskite $CaRuO_3$: ferromagnetism reduction. Solid State Sci 2010;12:2003–9.

[40] Keawpark N, Tu R, Goto T. Thermoelectricitiy of $CaIrO_3$ ceramics prepared by spark plasma sintering. J Cera Soc Jpn 2009;117(4):466–9.

[41] Ahsan Zeb M, Kee HY. Interplay between spin-orbit coupling and Hubbard interactions in $SrIrO_3$ and related Pbnn perovskite oxides. Phys Rev B 2012;86:085149.

[42] Nie YF, King PDC, Kim CH, Uchida M, Wei HI, Faeth BD, Ruf JP, Ruff JPC, Xie L, Pan X, Fennie CJ, Schlom DG, Shen KM. Interplay of spin-orbit interactions, dimensionality, and octahedral rotations in semimetallic $SrIrO_3$. Phys Rev Lett 2015;114:016401.

[43] Zhao JG, Yang LX, Yu Y, Li FY, Ru RC, Fang Z, Chen LC, Jin CQ. High-pressure synthesis of orthorhombic $SrIrO_3$ perovskite and its positive magnetoresistance. J Appl Phys 2008;103:103706.

[44] Blanchard PER, Reynolds E, Kennedy BJ, Kimpton JA, Avdeev M, Belik AA. Anomalous thermal expansion in orthorhombic perovskite $SrIrO_3$: interplay between spin-orbit coupling and the crystal lattice. Phys Rev B 2014;89:214106.

[45] Matsuno J, Ihara K, Yamamura S, Wadati H, Ishii K, Vijay Shankar V, Kee HY, Takagi H. Engineering spin-orbital magnetic insulator by tailoring superlattice. ArXiv: 1401.1066. 2014.

[46] Qasim I, Kennedy BJ, Avdeev M. Synthesis, structures and properties of transition metal doped $SrIrO_3$. J Mater Chem A 2013;1:3127–32.

[47] Bremholm M, Yim CK, Hirai D, Climent-Pascual E, Xu Q, Zandberen HW, Ali MN, Cava RJ. Destabilization of the 6H-$SrIrO_3$ polymorph through partial substitution of zinc and lithium. J Mater Chem 2012;22:16431–6.

[48] Wu FX, Zhou J, Zhang LY, Chen YB, Zhang ST, Gu ZB, Yao SH, Chen YF. Metal-insulator transition in $SrIrO_3$ with strong spin-orbit interaction. J Phys: Condens Matter 2013;25:125604.

[49] Chen Y, Lu YM, Kee HY. Topological crystalline metal in orthorhombic perovskite iridates. Nat Commun 2015;6:6593.

[50] Cheng JG, Zhou JS, Goodenough JB, Matsubayashi K, Uwatoko Y. Weak ferromagnetism in the orthorhombic perovskite $SrIr_{0.8}Sn_{0.2}O_3$. JPS Conf Proc 2014;3:013014.

[51] Nakano T, Terasaki I. Giant nonlinear conduction and Thyristor-like negative differential resistance in $BaIrO_3$ single crystal. Phys Rev B 2006;73:195106.

[52] Laguna-Marco MA, Haskel D, Souza-Neto N, Lang JC, Krishnamurthy VV, Chikara S, Cao G, Van Veenendaal M. Orbital magnetism and spin-orbit effects in the electronic structure of $BaIrO_3$. Phys Rev Lett 2010;105:216407.

[53] Ju WW, Liu GQ, Yang ZQ. Exotic spin-orbital Mott insulating states in $BaIrO_3$. Phys Rev B 2013;87:075112.

[54] Powell AV, Battle PD. A time-of-flight powder neutron diffraction study of non-stoichiometry in barium iridates $BaIrO_{3-\delta}$. J Alloy Comp 1996;232:147.

[55] Zhao JG, Yang LX, Yu Y, Li FY, Yu RC, Jin CQ. Structural and physical properties of the 6M $BaIrO_3$: a new metallic iridate synthesized under high pressure. Inorg Chem 2009;48:4290–4.

[56] Zhao JG, Yang LX, Yu Y, Li FY, Yu RC, Jin CQ. Physical properties of the 5M $BaIrO_3$: a new weak ferromagnetic iridate synthesized under high pressure. Solid State Commun 2010;150:36–9.

[57] Goodenough JB, Kafalas JA, Longo JM. High-Pressure Synthesis: Preparative Methods in Solid State Chemistry. New York and London: Academic Press, Inc.; 1972.

[58] Kini NS, Bentien A, Ramakrishnan S, Geibel C. Specific heat and transport study of the co-existence of chage-density-wave and weak ferromagnetism in $BaIrO_3$. Physica B 2005;359–361:1264.

[59] Maiti K, Singh RS, Medicherla VRR, Rayaprol S, Sampathkumaran EV. Origin of charge density wave formation in insulators from high resolution photoemission study of $BaIrO_3$. Phys Rev Lett 2005;95:016404.

[60] Brooks ML, Blundell SJ, Lancaster T, Hayes W, Pratt FL, Frampton PPC, Battle PD. Unconventional magnetic properties of the weakly ferromagnetic metal $BaIrO_3$. Phys Rev B 2005;71:220411(R).

[61] Laguna-Marco MA, Fabbris G, Souza-Neto N, Chikara S, Schilling JS, Cao G, Haskel D. Different response of transport and magnetic properties of $BaIrO_3$ to chemical and physical pressure. Phys Rev B 2014;90:014419.

[62] Cao G, Lin XN, Chikara S, Durairaj V, Elhami E. High-temperature weak ferromagnetism on the verge of a metallic state: impact of dilute Sr doping on $BaIrO_3$. Phys Rev B 2004;69:174418.

[63] Korneta OB, Chikara S, Parkin S, DeLong LE, Schlottmann P, Cao G. Pressure-induced insulating state in $Ba_{1-x}R_xIrO_3$ (R=Gd, Eu) single crystals. Phys Rev B 2010;81:045101.